Buoyancy and Wind-Driven Convection at Mixed Layer Density Fronts

JOHN R. TAYLOR AND RAFFAELE FERRARI

Department of Earth, Atmospheric and Planetary Sciences, Massachusetts Institute of Technology, Cambridge, Massachusetts

(Manuscript received 21 September 2009, in final form 7 January 2010)

ABSTRACT

In this study, the influence of a geostrophically balanced horizontal density gradient on turbulent convection in the ocean is examined using numerical simulations and a theoretical scaling analysis. Starting with uniform horizontal and vertical buoyancy gradients, convection is driven by imposing a heat loss or a destabilizing wind stress at the upper boundary, and a turbulent layer soon develops. For weak lateral fronts, turbulent convection results in a nearly homogeneous mixed layer (ML) whose depth grows in time. For strong fronts, a turbulent layer develops, but this layer is not an ML in the traditional sense because it is characterized by persistent horizontal and vertical gradients in density. The turbulent layer is, however, nearly homogeneous in potential vorticity (PV), with a value near zero. Using the PV budget, a scaling for the depth of the turbulent low PV layer and its time dependence is derived that compares well with numerical simulations. Two dynamical regimes are identified. In a convective layer near the surface, turbulence is generated by the buoyancy loss at the surface; below this layer, turbulence is generated by a symmetric instability of the lateral density gradient. This work extends classical scalings for the depth of turbulent boundary layers to account for the ubiquitous presence of lateral density gradients in the ocean. The new results indicate that a lateral density gradient, in addition to the surface forcing, can affect the stratification and the rate of growth of the surface boundary layer.

1. Introduction

The upper ocean is characterized by a surface mixed layer (ML) that is weakly stratified in density compared to the ocean interior. It is generally assumed that the weak stratification is maintained by vertical mixing powered by atmospheric winds and air–sea buoyancy fluxes and that the depth of the ML is set through a competition between surface fluxes and preexisting vertical stratification. The ML, however, is not horizontally homogeneous, and horizontal density gradients can substantially modify its depth and structure (e.g., Tandon and Garrett 1995; Marshall and Schott 1999; Thomas 2005; Boccaletti et al. 2007).

The primary objective of this paper is to examine the influence of a horizontal density gradient on convection in the ocean. We will refer to the general situation of convection into a baroclinic fluid as ''slantwise convection'' to distinguish this case from classical ''upright convection,'' where horizontal density gradients are unimportant. Thorpe and Rotunno (1989) objected to the term slantwise convection, noting that the turbulent heat flux can reverse sign compared to classical convection. Here, we will use the term slantwise convection but will distinguish two limits based on the sign of the buoyancy flux. Near the surface, a ''convective layer'' occurs where the turbulent buoyancy flux is responsible for most of the turbulent kinetic energy (TKE) production. Below this layer, a second regime can arise, which we will call ''forced symmetric instability'' (forced SI), where shear production takes over as the primary source of TKE.

SI describes growing perturbations in a rotating, stratified fluid that are independent of the alongfront direction. Consider a fluid with a uniform horizontal and vertical buoyancy gradient; that is, $N^2 = db/dz =$ constant and $M^2 = db/dx =$ constant, where $b = -g\rho/\rho_0$ is the buoyancy, ρ is the density, ρ_0 is a reference density, and g is the gravitational acceleration. Also, suppose that the lateral stratification is in thermal wind balance with a meridional flow V_G; that is, $dV_G/dz = M^2/f$. It can

Corresponding author address: Raffaele Ferrari, Dept. of Earth, Atmospheric and Planetary Sciences 54-1420, Massachusetts Institute of Technology, 77 Massachusetts Ave., Cambridge, MA 02139. E-mail: rferrari@mit.edu

DOI: 10.1175/2010JPO4365.1

be shown[1] that this basic state is unstable to inviscid SI when the bulk Richardson number $\mathrm{Ri}_B \equiv N^2/(dV_G/dz)^2 < 1$ (see, e.g., Stone 1966). The most unstable mode of inviscid SI has streamlines that are aligned with the isopycnal surfaces. Thorpe and Rotunno (1989) and Taylor and Ferrari (2009) found that turbulence can rapidly neutralize SI through enhanced boundary fluxes and/or entrainment of stratified fluid from a neighboring region. Taylor and Ferrari (2009) identified a secondary Kelvin–Helmholtz instability that develops from the along-isopycnal shear associated with SI.

To describe the dynamical role of a balanced lateral density gradient, it is useful to introduce the concept of potential vorticity (PV). The Ertel PV q can be defined as

$$q = (f\,\mathbf{k} + \boldsymbol{\omega}) \cdot \nabla b, \tag{1}$$

where $\boldsymbol{\omega} = \nabla \times \mathbf{u}$ is the relative vorticity and f is the constant Coriolis parameter under the f-plane approximation. Here, f is assumed to be positive without loss of generality. For a fluid with constant N^2 and M^2 and a velocity in thermal wind balance, $q = fN^2 - M^4/f$. In a ML with a spatially uniform velocity and density, the PV is zero. When $M^2 \neq 0$, the PV can become negative through the baroclinic term $-M^4/f$.

A balanced state with a negative PV is unstable. Convective instabilities develop when $N^2 < 0$ or equivalently $\mathrm{Ri}_B < 0$. Other instabilities develop when N^2 is positive, but the baroclinic term is large enough to make the PV negative. Kelvin–Helmholtz shear instability develops when $0 < \mathrm{Ri}_B < 0.25$, whereas SI is the most unstable mode when $0.25 < \mathrm{Ri}_B < 0.95$ (Stone 1966). Consider a surface forcing that removes PV from the ocean until regions of negative PV develop. Conditions will then be favorable for convective and/or SI, which will attempt to return the fluid to a neutral state by eliminating the regions of negative PV. A low PV region ($q \simeq 0$) can therefore be thought of as a generalization of the surface ML, which includes the possibility of horizontal density gradients and nonzero stratification (Marshall and Schott 1999). In light of this, we will refer to the region affected by surface forcing as the low PV layer instead of the mixed layer. In section 6, scalings are derived for the growth and structure of the low PV layer, which generalize traditional expressions for the growth of the surface ML.

[1] The stability criterion based on the bulk Richardson number applies only when there is no vertical vorticity associated with the basic state. A more general criterion for symmetric instability is $\mathrm{Ri}_B = N^2/|\partial \mathbf{U}_G/\partial z|^2 < f/(f + \partial V_G/\partial x - \partial U_G/\partial y)$ (Haine and Marshall 1998).

Haine and Marshall (1998) described numerical simulations of slantwise convection where a horizontal density gradient was formed by spatial variations in the surface cooling. They found that the isopycnals aligned with surfaces of constant absolute momentum, $\mathcal{M} = (M^2/f)z + fx$, implying a nonzero vertical stratification. Straneo et al. (2002) also examined slantwise convection in a parameter range consistent with deep convection. They used parcel theory to predict the influence of M^2 on the convective layer depth and zero PV. Straneo et al. (2002) focused on convection at high latitudes and considered large surface buoyancy fluxes and relatively weak horizontal density gradients, whereas in Haine and Marshall (1998) the horizontal density gradient was inherently linked to the magnitude of the surface buoyancy flux, so that strong horizontal density gradients occurred only for strong forcing. In the ocean, strong fronts can form via frontogenesis on scales much smaller than the atmospheric forcing. In this paper, we vary M^2 and the surface heat flux independently and find that the development and structure of the low PV layer enter in a new dynamical regime for moderate heat fluxes and strong, preexisting oceanic fronts.

The primary goals of this paper are to determine when and how a horizontal density gradient affects turbulent convection using the numerical simulations outlined in section 2. Sections 3–5 describe features of convection at a density front, section 6 presents a scaling analysis for the depth of the low PV layer, and section 7 uses a scaling analysis to predict the relative importance of the horizontal density gradient during convective events and the conditions when forced SI can be expected. Section 9 offers conclusions.

2. Model setup

To examine the influence of a horizontal density gradient on turbulent convection, we have conducted nonlinear numerical simulations in the idealized geometry illustrated in Fig. 1. The front is represented by a constant lateral buoyancy gradient superimposed on a constant vertical stratification. ML fronts have been shown to develop baroclinic instability through the formation of submesoscale meanders with scales close to the surface deformation radius of $O(10\ \mathrm{km})$ (Boccaletti et al. 2007). Because resolving submesoscale instabilities and three-dimensional (3D) convective motions on scales of $O(1\ \mathrm{m})$ would be computationally prohibitive, we limit the domain size to horizontal scales smaller than the deformation radius and focus on the influence of the front on convectively driven turbulence.

The buoyancy and velocity fields are decomposed into departures from a constant background state,

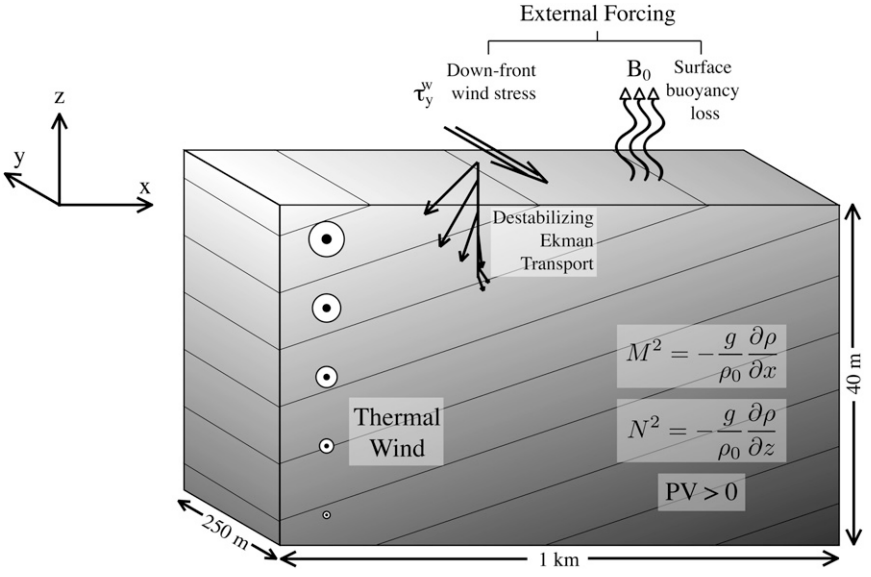

FIG. 1. Schematic of the numerical simulation domain. The domain size given is for the 3D simulations; 2D simulations use a vertical domain size of 80 m and neglect variations in the y direction.

$$b_T(x, y, z, t) = b(x, y, z, t) + M^2 x,$$
$$\mathbf{u}_T = \mathbf{u}(x, y, z, t) + V_G(z)\mathbf{j}, \quad dV_G/dz = M^2/f, \tag{2}$$

where the basic state is given by a constant lateral buoyancy gradient M^2 in thermal wind balance with the sheared velocity V_G. The momentum and buoyancy equations for the perturbations are then solved numerically,

$$\frac{\partial u}{\partial t} + \mathbf{u}_T \cdot \nabla u - fv = -\frac{1}{\rho_0}\frac{\partial p}{\partial x} + \nu\nabla^2 u, \tag{3}$$

$$\frac{\partial v}{\partial t} + \mathbf{u}_T \cdot \nabla v + w\frac{dV_G}{dz} + fu = -\frac{1}{\rho_0}\frac{\partial p}{\partial y} + \nu\nabla^2 v, \tag{4}$$

$$\frac{\partial w}{\partial t} + \mathbf{u}_T \cdot \nabla w = -\frac{1}{\rho_0}\frac{\partial p}{\partial z} + b + \nu\nabla^2 w, \tag{5}$$

$$\frac{\partial b}{\partial t} + \mathbf{u}_T \cdot \nabla b + uM^2 = \kappa\nabla^2 b, \quad \text{and} \tag{6}$$

$$\nabla \cdot \mathbf{u} = 0. \tag{7}$$

Derivatives in the horizontal directions are calculated with a pseudospectral method, and vertical derivatives are approximated with second-order finite differences. The time-stepping algorithm uses the Crank–Nicolson method for the diffusive terms involving vertical derivatives and a third-order Runge–Kutta method for the remaining terms. Details of the numerical method are given in Taylor (2008) and Bewley (2010). Periodic boundary conditions are applied to the perturbation quantities $\mathbf{u}$ and b in the horizontal directions. Because the background buoyancy is a function of x, enforcing periodicity effectively maintains a constant buoyancy difference across the computational domain (although the local buoyancy gradient is free to evolve in time). As a result, we are not able to capture the temporal evolution of the front on large scales.

For simplicity, the simulations all begin with a uniform vertical and horizontal buoyancy gradient and a velocity field in thermal wind balance,

$$b_T(t = 0) = N_0^2 z + M^2 x, \quad \mathbf{u}_T(t = 0) = V_G(z)\mathbf{j}, \tag{8}$$

where N_0 is the constant initial buoyancy frequency. Turbulent convection is forced by applying either a uniform surface buoyancy flux $B_0 \equiv \kappa\partial b/\partial z|_{z=0}$ or a "down-front" wind stress $\tau_y^w/\rho_0 = \nu\partial v/\partial z|_{z=0} + \nu\, dV_G/dz$, which will be discussed in section 4. To minimize inertial oscillations that would be generated by impulsively forcing, the amplitude of the surface forcing is increased linearly from zero during the first day of simulation time. In the absence of a wind stress, a free-slip boundary condition is applied to $\mathbf{u}_T$ at $z = 0$. To speed the transition to a turbulent state, random fluctuations are added to the velocity field with an amplitude of 1 mm s^{-1} with zero mean and a white spectrum in Fourier space. To examine the impact of the horizontal density gradient on convection, M^2, B_0, and τ^w are varied over the set of simulations described in Table 1. Using a thermal expansion coefficient and heat capacity of 1.65×10^{-4} °C^{-1} and 4×10^3 J kg^{-1} °C^{-1}, a typical imposed surface

TABLE 1. Simulation parameters and bulk estimates. All simulations have $f = 1 \times 10^{-4}$ (s^{-1}) and $N_0^2 = 9 \times 10^{-5}$ s^{-2}. The entrainment coefficients are $\alpha = \alpha_{res} + \alpha_{SGS} = [\langle w'b' \rangle_{(z=-H)} - \kappa \langle N^2 \rangle_{(z=-H)}/(B_0 + B_{wind})] - \kappa_{SGS} \langle N^2 \rangle_{(z=-H)}/(B_0 + B_{wind})$ and $\beta \equiv [(\tau_y^w M^2/\rho_0 f) - M^2 \int_{-H}^{0} \langle u \rangle \, dz]/(B_0 + B_{wind})$. The entrainment coefficients were averaged in time at the depth where $\langle q \rangle = 0.99 Q_0$. This location was chosen because the definition of $H(t)$ used in section 6 (the location where the PV flux is identically zero) produces a very noisy time series.

Name	M^2 ($s^{-2} \times 10^{-7}$)	B_0 (m^2 $s^{-3} \times 10^{-8}$)	$M^2 \tau_y^w/(\rho_0 f)$ (m^2 $s^{-3} \times 10^{-8}$)	α_{res}	α_{SGS}	β
2D_1	0	−4.24	0	0.08	0.22	0
2D_2	−4.24	−4.24	0	0.00	0.21	−0.09
2D_3	−2.12	−4.24	0	0.02	0.21	−0.04
2D_4	−8.48	−4.24	0	0.00	0.21	−0.20
2D_5	−4.24	−8.48	0	0.01	0.11	−0.03
2D_6	−4.24	−2.12	0	0.00	0.42	−0.12
2D_7	−4.24	0	−4.24	0.01	0.21	−0.04
3D_1	0	−4.24	0	0.00	0.32	0
3D_2	−4.24	−4.24	0	0.00	0.29	−0.05

buoyancy flux of $B_0 = -4.24 \times 10^{-8}$ m^2 s^{-3} corresponds to a surface heat loss of about 100 W m^{-2}.

The entire suite of simulations has been run in 2D in an x–z plane neglecting all variations in the alongfront (y) direction but retaining the full 3D velocity field (this type of simulation is referred to as 2½*D* by some authors). To test the impact of neglecting variations in the y direction, two of the simulations have been repeated in 3D, which will be described in section 5. For the 2D simulations, the computational domain size is $L_x = 1000$ m, and $L_z = 100$ m with $N_x = 1024$ and $N_z = 128$ grid points. The grid is uniform in the x direction and stretched in the z direction with a minimum grid spacing of $\Delta z_{min} = 0.17$ m at $z = 0$ and a maximum of $\Delta z_{max} = 1.4$ m at $z = -100$ m. To allow internal waves to escape from the bottom of the domain, a Rayleigh damping (or "sponge" layer) is applied in the region from -100 m $< z < -80$ m, where the mean velocity and buoyancy profiles are relaxed toward their initial state. The damping function takes the form $\partial b/\partial t = \cdots - \sigma[(-80 - z)/20]^2 (b - N_0^2 z)$ with $\sigma = 0.005$.

3. 2D simulations of upright and slantwise convection

a. Buoyancy budget

The evolution of the mean buoyancy is described by

$$\frac{\partial \langle b \rangle}{\partial t} = -\frac{\partial}{\partial z} \langle w'b' \rangle - \langle u \rangle M^2 + \kappa \frac{\partial^2 \langle b \rangle}{\partial z^2}, \qquad (9)$$

where $\langle \cdot \rangle$ denotes an average over the x and y plane and for one inertial period in time and primes denote a departure from the mean state. The horizontal convergence of the buoyancy flux is identically zero and does not appear in Eq. (9), because the perturbation quantities are periodic in x and y. For upright convection when $M^2 = 0$, the mean buoyancy can only be changed through a divergence or convergence in the vertical buoyancy flux. When a background horizontal density gradient is present, the mean advection term $\langle u \rangle M^2$ can also alter the mean buoyancy profile.

The temporal evolution of the mean buoyancy frequency $\langle N^2 \rangle = d\langle b \rangle/dz$ with and without a background horizontal density gradient is shown in Fig. 2. The initial stratification N_0 and the surface buoyancy flux B_0 are identical in both cases. Simulation $2D_1$ represents classical upright convection without a mean horizontal density gradient. In this case, the ML grows as the square root of time, as expected for a constant surface buoyancy flux (Turner 1973). Simulation $2D_2$ has a horizontal density gradient $M^2 = -4.24 \times 10^{-7}$ s^{-2}, which represents a relatively strong front. As in simulation $2D_1$, a turbulent layer develops near the surface and grows in time. However, in simulation $2D_2$ this layer is associated with a weak but nonzero vertical stratification.

Profiles of the mean buoyancy frequency $\langle N^2 \rangle$ are shown in Fig. 3a at $t = 15$ days for a range of values of M^2 and B_0. The low PV layer generally coincides with the region where $\langle N^2 \rangle < N_0^2$ ($N_0^2 = 9 \times 10^{-5}$ s^{-2} in all cases). The dependence of the low PV layer depth on the external parameters will be addressed in section 6. By comparing with the parameter values listed in Table 1, we see that the stratification in the low PV layer depends on the background horizontal buoyancy gradient M^2. As shown in Fig. 3b, the stratification in the low PV layer scales in such a way as to keep $Ri_B \simeq 1$. Note that the region with $Ri_B \simeq 1$ has not yet formed in simulation $2D_3$ but is seen at later times.

Along with the mean stratification profiles, the leading order terms in the buoyancy budget are dramatically altered by the presence of a horizontal density gradient. The terms in Eq. (9) are shown in Fig. 4 at $t = 15$ days for simulations $2D_1$ and $2D_2$. In simulation $2D_1$, with $M^2 = 0$, the decrease in buoyancy is balanced by the vertical

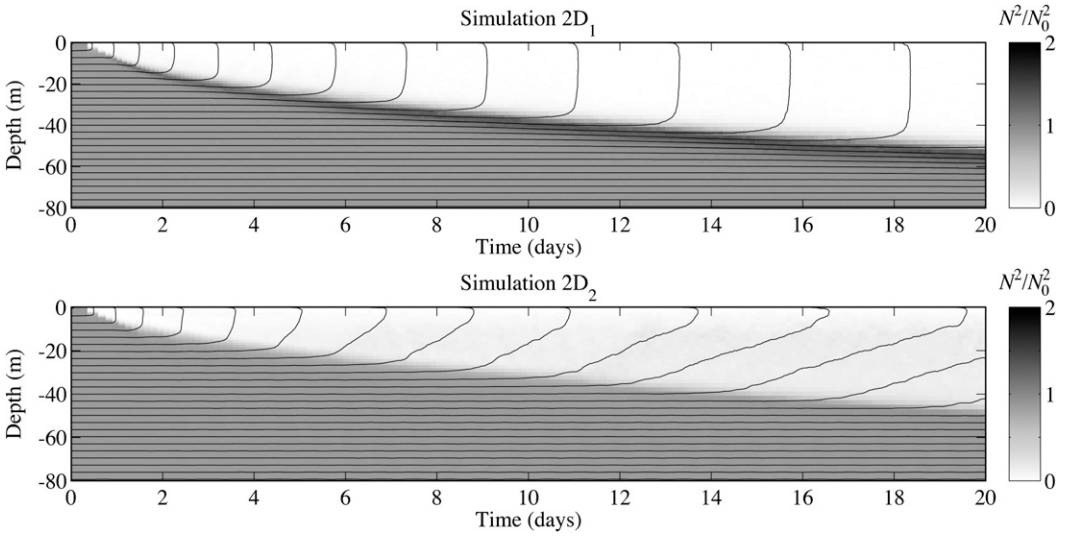

FIG. 2. Evolution of the buoyancy frequency normalized by the initial value for a simulation of upright convection (simulation $2D_1$) and convection at a density front (simulation $2D_2$). Contour lines of the x-averaged buoyancy are also shown. The initial buoyancy frequency and the imposed heat flux are the same in both cases.

derivative of the buoyancy flux. Both are nearly constant in the low PV layer, indicating that the buoyancy flux profile is linear in z. Terms involving the constant diffusivity κ play a role at the top and bottom of the low PV layer but not in the interior and are not shown. In contrast, for slantwise convection in simulation $2D_2$, the divergence of the buoyancy flux is large for $z \gtrsim -10$ m, and lateral advection roughly balances the decrease in the mean buoyancy for $z \gtrsim -10$ m.

b. Momentum budget

The mean velocity profiles for simulation $2D_2$ are shown in Fig. 5 after $t = 15$ days when the low PV layer depth is about 40 m. Below the low PV layer, the mean

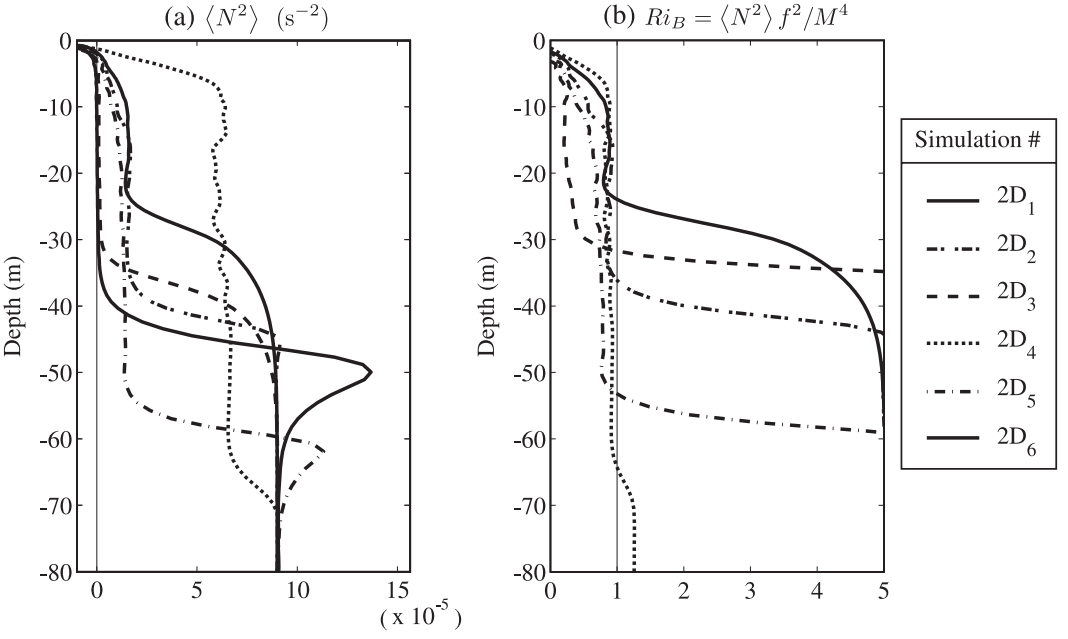

FIG. 3. (a) Buoyancy frequency and (b) bulk Richardson number averaged in x and for 1 inertial period centered at $t = 15$ days.

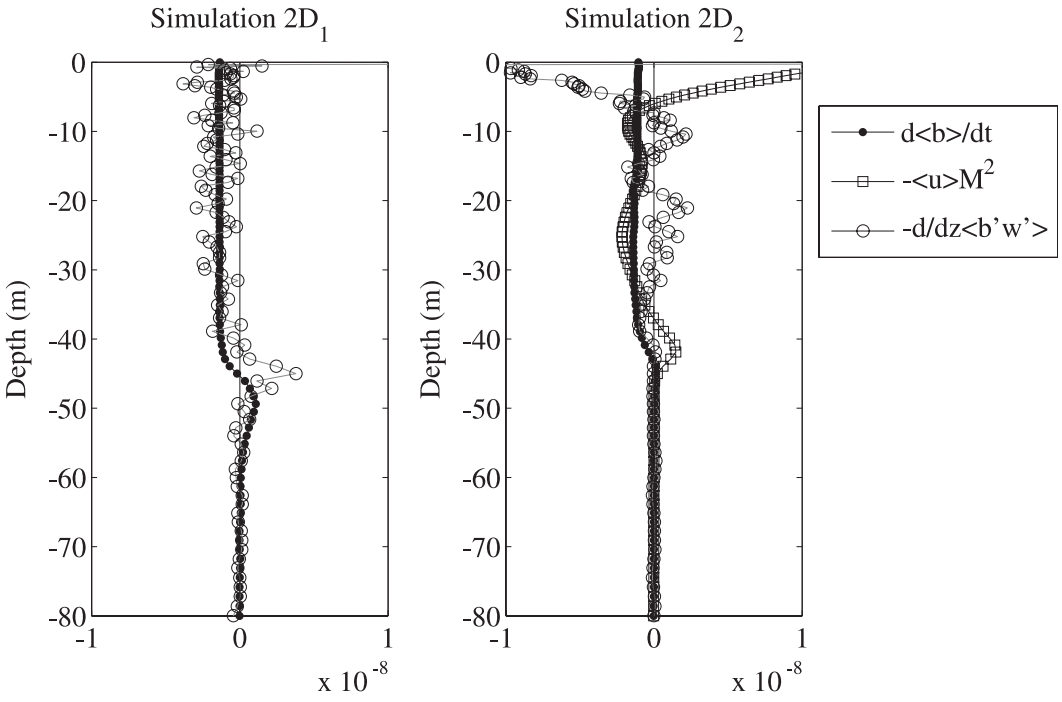

FIG. 4. Mean buoyancy budget for (left) upright convection (simulation $2D_1$) and (right) slantwise convection (simulation $2D_2$). Each term has been averaged in the x direction and for one inertial period in time, centered at $t = 15$ days. The statistical noise in the buoyancy flux divergence is the result of a relatively small sample size. The buoyancy flux and mean velocity were sampled every 100 time steps and then averaged over the appropriate time window.

velocity is unchanged from the initial state: namely, $\langle u \rangle = 0$ and $\partial \langle v_T \rangle / \partial z = M^2/f$. Inside the low PV layer, viscous and turbulent momentum stresses lead to an ageostrophic mean flow that is well described by an Ekman balance:

$$f\langle u \rangle \simeq -\frac{\partial \langle v'w' \rangle}{\partial z} + \nu \frac{\partial^2 \langle v \rangle}{\partial z^2} \quad \text{and}$$
$$-f\langle v \rangle \simeq -\frac{\partial \langle u'w' \rangle}{\partial z} + \nu \frac{\partial^2 \langle u \rangle}{\partial z^2}. \tag{10}$$

The turbulent stress terms are shown in Figs. 5a,b and nearly balance the mean velocity in the low PV layer, with the exception of a thin viscous layer near $z = 0$. The mean velocity vectors are shown in Fig. 5c as a function of depth. The shape of the mean velocity profile is reminiscent of a turbulent Ekman spiral, with the addition of a linear thermal wind resulting from the background shear dV_G/dz.

Instantaneous snapshots of the velocity and density fields are shown in Fig. 6. Positive and negative values of the streamfunction in the x–z plane are shown in black and white contour lines, and density is shown using gray-scale shading. Note that there is a nonzero alongfront velocity $\langle v \rangle$ that is not shown. Striking qualitative differences are visible in the flow with a front ($2D_2$) and without a front ($2D_1$). In simulation $2D_1$, upright convection cells extend throughout the low PV layer. The density in the low PV layer is nearly uniform, and entrained patches of thermocline fluid can be seen at the ML base. In contrast, in simulation $2D_2$, the streamlines are roughly aligned with the isopycnals and small-scale overturns are visible in the density field. Qualitatively, this is very similar to the symmetrically unstable front described by Taylor and Ferrari (2009).

c. PV budget

In upright convection, when $M^2 = 0$, the mean buoyancy equation is decoupled from the equations for the mean horizontal velocity, and Eq. (9) can be closed quite accurately by assuming that $\langle w'b' \rangle$ matches the imposed buoyancy flux at the surface and decreases linearly to zero over the ML depth. However, when $M^2 \neq 0$ and $f \neq 0$, the equations for $\langle b \rangle$, $\langle u \rangle$, and $\langle v \rangle$ are coupled. In this case, the problem is significantly more difficult to approach analytically because the buoyancy flux $\langle w'b' \rangle$ and the Reynolds stresses $\langle u'w' \rangle$ and $\langle v'w' \rangle$ need to be modeled to close the mean momentum and buoyancy equations.

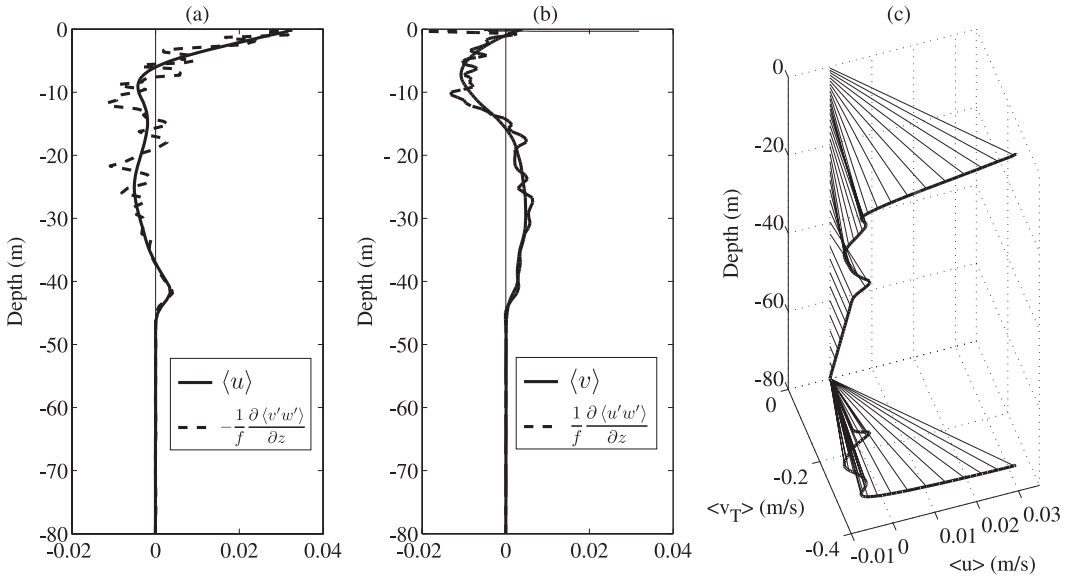

FIG. 5. Simulation $2D_2$: (a) Mean cross-front velocity, (b) mean alongfront velocity, and (c) hodograph of the mean velocity vectors (all m s^{-1}). All quantities are averaged in x and for 1 inertial period centered at $t = 15$ days. Dashed lines in (a),(b) illustrate the turbulent Ekman balance given in Eq. (10).

Progress can be made by combining the momentum and buoyancy equations into a single equation for a conserved scalar, the PV, which is defined in Eq. (1). The evolution for the mean PV can be written as

$$\left\langle \frac{Dq}{Dt} \right\rangle = \frac{\partial \langle q \rangle}{\partial t} + \frac{\partial \langle J^z \rangle}{\partial z} = 0, \tag{11}$$

where J^z is the vertical component of the PV flux vector (Thomas 2005; Marshall and Nurser 1992)

$$\mathbf{J} = q\mathbf{u} + \nabla b \times \boldsymbol{\mathcal{F}} - \mathcal{D}(f\,\mathbf{k} + \boldsymbol{\omega}) \tag{12}$$

and $\mathcal{D} \equiv \kappa \nabla^2 b$ and $\boldsymbol{\mathcal{F}} \equiv \nu \nabla^2 \mathbf{u}$ are F the diabatic and frictional terms appearing in the buoyancy and momentum equations. Outside diffusive and viscous boundary layers, the diabatic and frictional terms can be neglected in Eq. (11), and PV is a conserved scalar. Although the PV exhibits large local fluctuations in the turbulent region, the mean PV provides a convenient way to describe the evolution of the flow with and without a horizontal density gradient.

The rate of PV destruction averaged over the low PV layer is set through the upper boundary condition. The upward PV flux at a rigid surface can be written

$$J_0^z = -\mathcal{D}(\boldsymbol{\omega} \cdot \mathbf{k} + f) + f \frac{d\mathbf{U}_G}{dz} \cdot \boldsymbol{\mathcal{F}}, \tag{13}$$

where $d\mathbf{U}_G/dz = f^{-1}\,\mathbf{k} \times \nabla b$ is the surface geostrophic shear (Thomas 2005). PV is extracted from the ocean when $J_0^z > 0$; for an inertially stable flow ($\boldsymbol{\omega} \cdot \mathbf{k} + f > 0$), a destabilizing surface buoyancy flux, $\mathcal{D} < 0$, will be associated with a loss of PV from the ocean. A PV loss could also result if a frictional force $\boldsymbol{\mathcal{F}}$ is applied with a component in the direction of the thermal wind $\mathbf{U}_G$ (Thomas 2005). This possibility will be explored in the next section.

The evolution of $\langle q \rangle$ as a function of depth and time is shown for all simulations in Figs. 7–9. Using the initial conditions in Eq. (1) (a uniform horizontal and vertical density gradient and a velocity in thermal wind balance), the PV at $t = 0$ is $Q_0 = fN_0^2 - M^4/f$. In each of the cases considered here, $Q_0 > 0$, so that the initial state is stable with respect to SI. Regardless of the value of M^2, the surface buoyancy loss causes a layer to develop with nearly zero PV. This low PV layer deepens in time, eroding the high PV thermocline. The simulations show that the rate of deepening depends on the surface buoyancy flux B_0 and the horizontal buoyancy gradient M^2.

If we consider the evolution of $\langle q \rangle$ away from viscous/diffusive boundary layers, on a time scale τ that is much larger than the inertial period ($\tau \gg f^{-1}$), we can show that at leading order in τf (see appendix)

$$\langle q'w' \rangle \simeq f \frac{\partial}{\partial z} \langle w'b' \rangle - M^2 \frac{\partial}{\partial z} \langle v'w' \rangle \simeq -f \frac{\partial \langle b \rangle}{\partial t}, \tag{14}$$

where we have also used the turbulent Ekman balance in Eq. (10). We have found that Eq. (14) holds even when $\tau = O(f)$ (see Fig. A1 and discussion in the appendix).

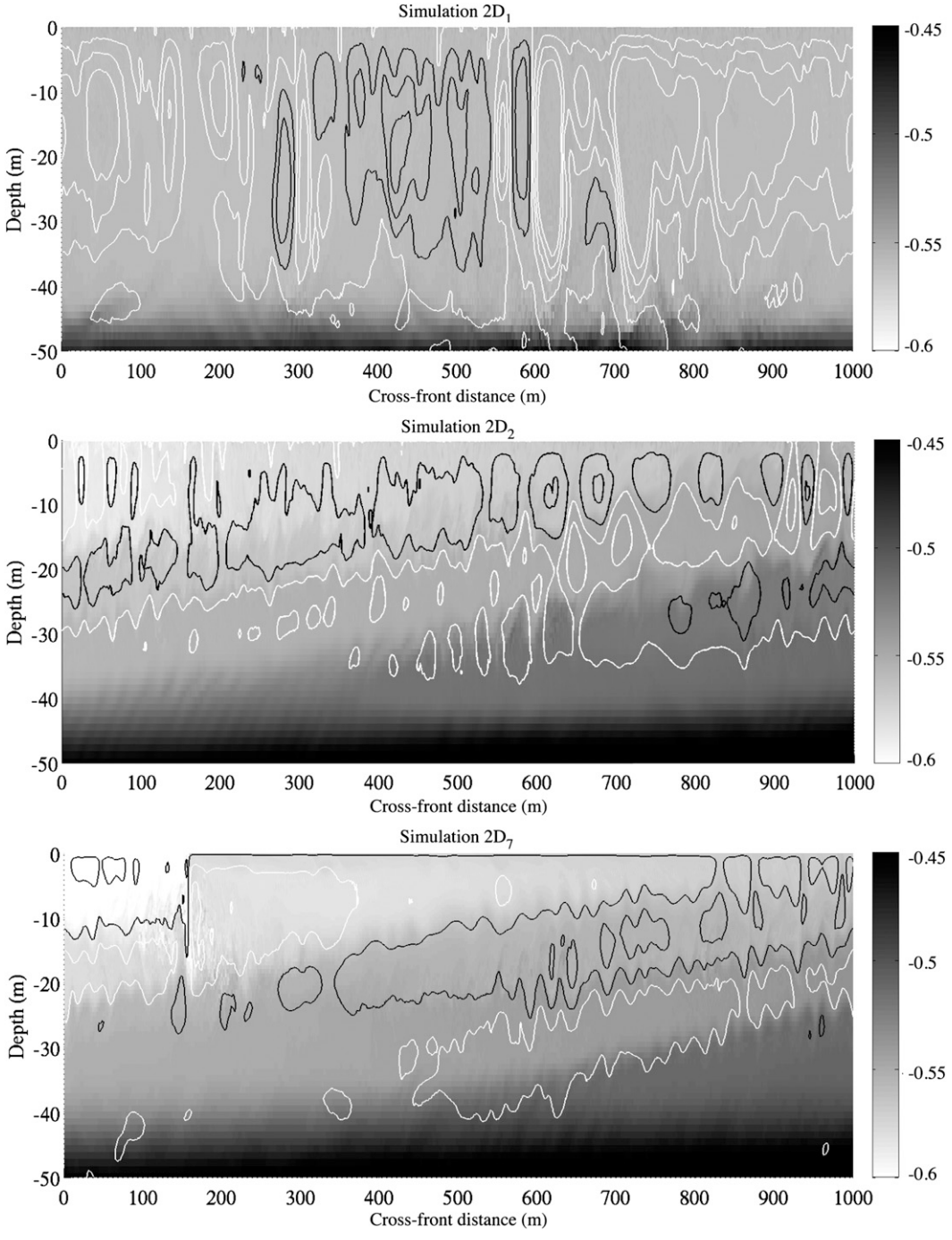

FIG. 6. Instantaneous u–w streamfunction (contour lines) and density (shading; kg m^{-3}) for simulations (top) $2D_1$, (middle) $2D_2$, and (bottom) $2D_7$ at $t = 15$ days. The streamfunction contour interval is 0.1 m^2 s^{-1} and black (white) contours indicate clockwise (counterclockwise) circulation.

Because it involves derivatives of fluctuating quantities, the instantaneous PV and PV flux contain high levels of statistical noise, even when averaged in x. In practice, we have found that it helps to integrate both in depth and time to smooth some of the statistical fluctuations. Using Eq. (14), and assuming that the turbulent fluxes vanish at a sufficient depth ($z = -\infty$), the integrated PV budget can be written

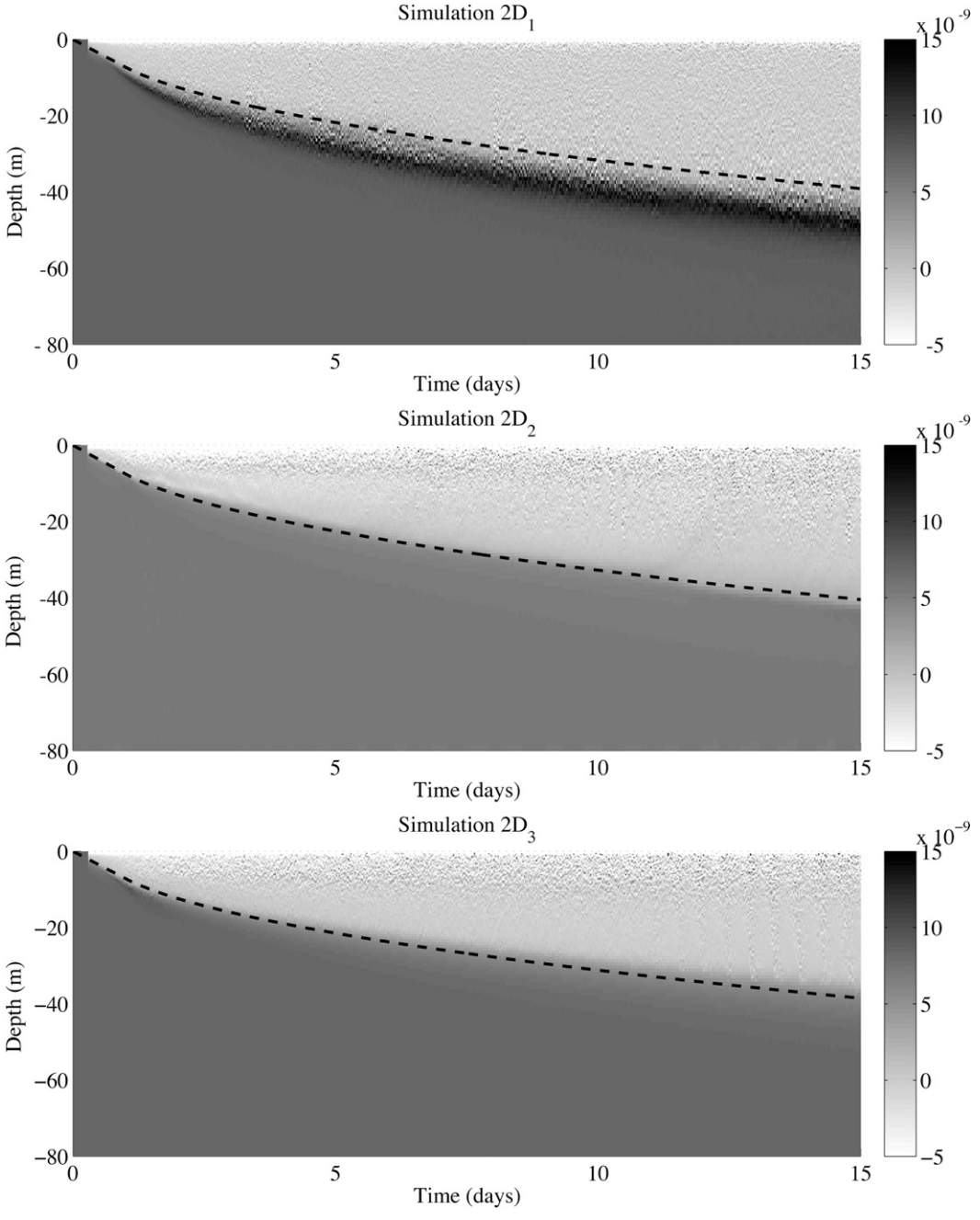

FIG. 7. Mean PV as a function of time and depth for simulations (top) $2D_1$, (middle) $2D_2$, and (bottom) $2D_3$. The dashed lines give the predicted zero PV layer depth from Eq. (23) as described in section 6.

$$\int_0^t \int_{-\infty}^z \frac{\partial \langle q \rangle}{\partial t}\, dz'\, dt' = -\int_0^t \langle q'w' \rangle|_z\, dt'$$

$$= -f \int_0^t \frac{\partial}{\partial z} \langle w'b' \rangle|_z\, dt'$$

$$- M^2 \int_0^t \left. \frac{\partial \langle v'w' \rangle}{\partial z} \right|_z dt'. \quad (15)$$

The terms in Eq. (15) are shown in Fig. 10 for simulations $2D_1$ and $2D_2$. The rate of change of the mean PV is well described by the terms in Eq. (14) throughout most of the low PV layer, although the diffusive buoyancy flux is nonnegligible at the base of the low PV layer and near the surface. Because $M^2 = 0$ in simulation $2D_1$, the buoyancy flux is responsible for all of the PV flux. In contrast, the momentum flux makes up the dominant

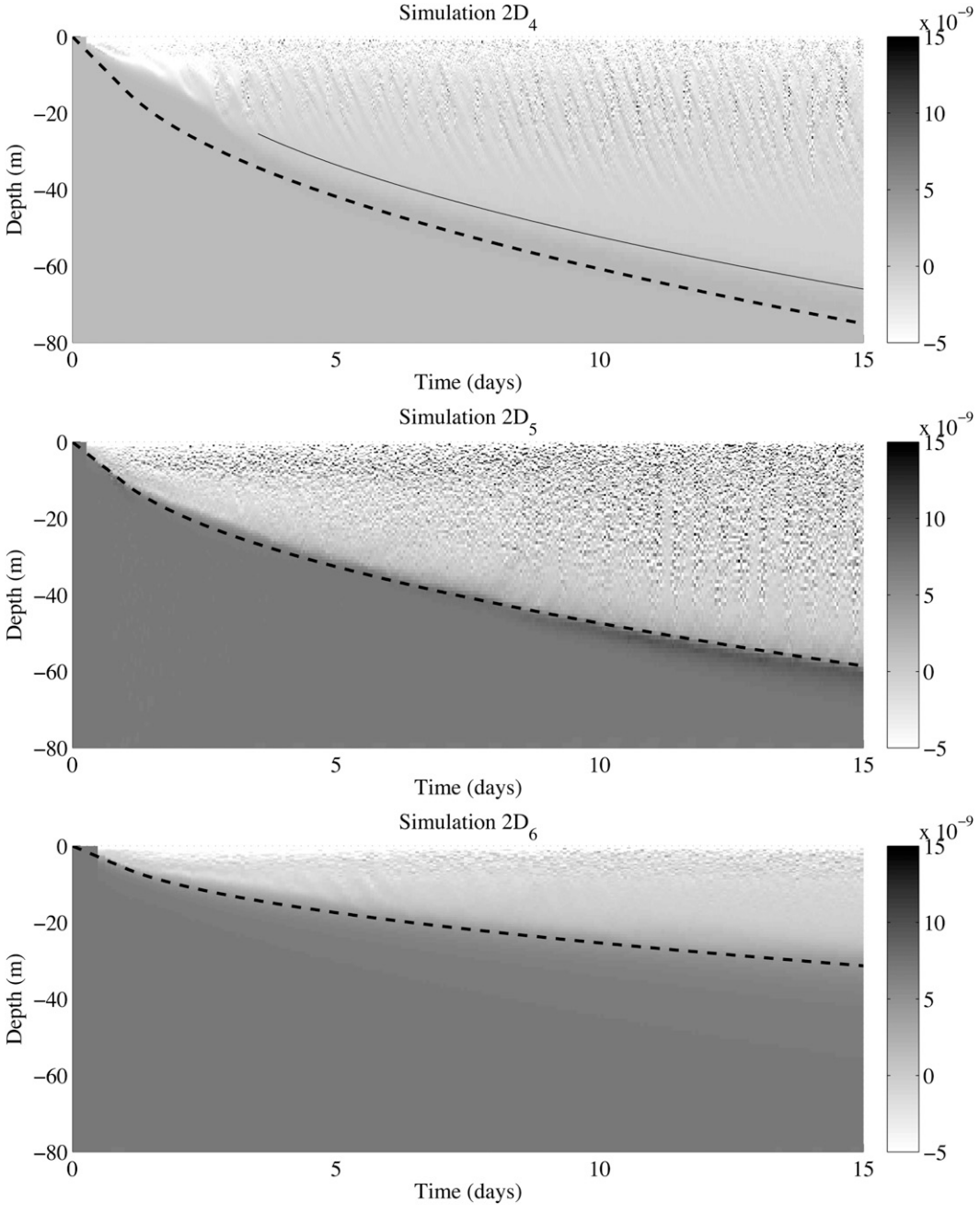

FIG. 8. As in Fig. 7, but for simulations $2D_4$, $2D_5$, and $2D_6$. (top) The solid line shows Eq. (23) evaluated starting from $t = 3$ days.

contribution to the PV flux for $z < -10$ m in simulation $2D_2$.

4. 2D simulations of wind-driven slantwise convection

Up until this point, we have discussed convection driven by an imposed surface buoyancy loss. In the ocean, a surface wind stress can also trigger convection. First, winds can increase the flux of heat from the ocean to the atmosphere, thereby modifying B_0 directly. Second, if there is a lateral density gradient and the wind blows downfront (i.e., the wind stress is aligned with the geostrophic shear associated with the density gradient), then the Ekman flow advects dense fluid over light, triggering convective overturns. Thomas and Lee (2005) showed

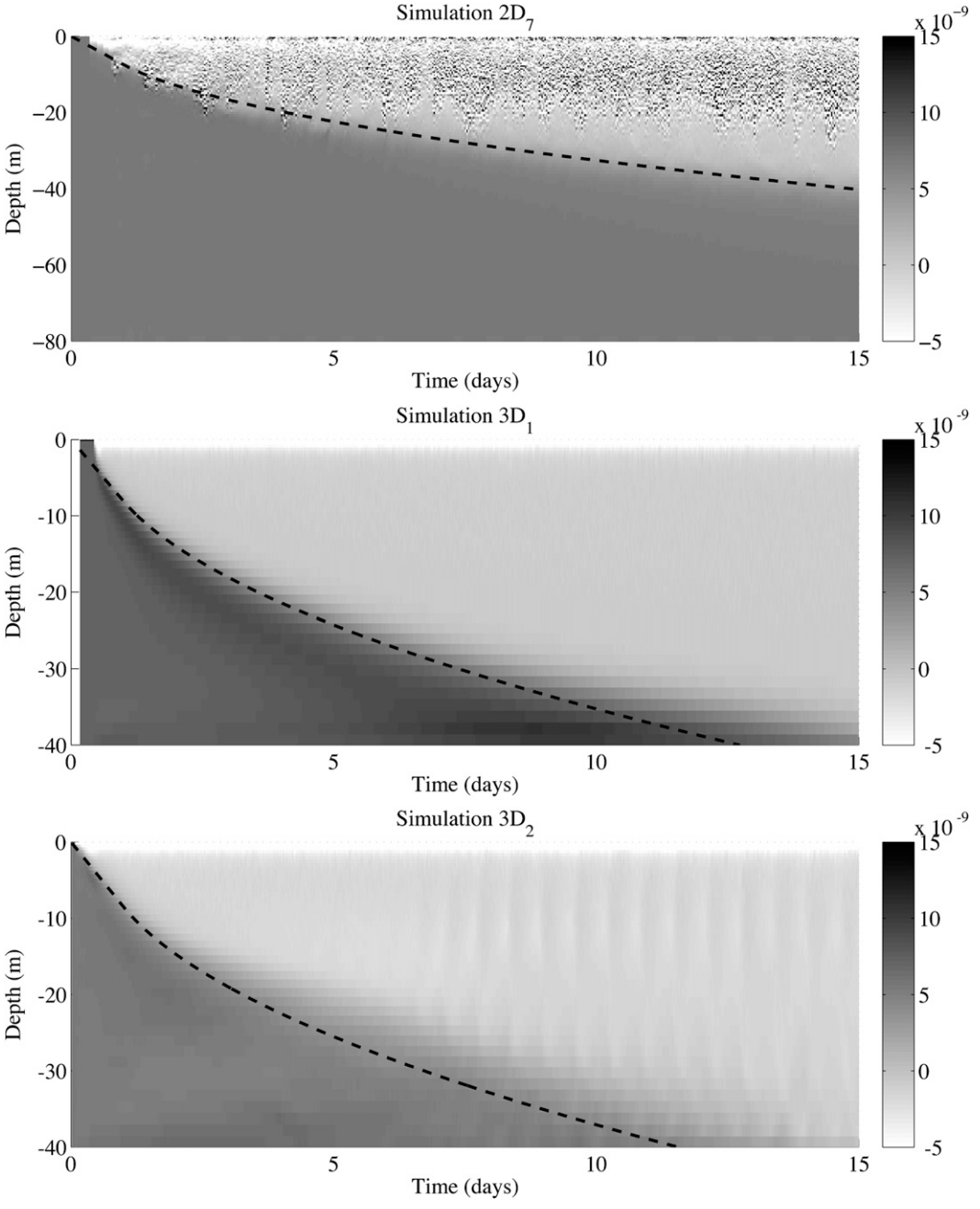

FIG. 9. As in Fig. 7, but for simulations $2D_7$, $3D_1$, and $3D_2$.

that the destabilization of the front by Ekman flow results in an effective wind-driven buoyancy flux given by

$$B_{\text{wind}} = -\int_{-H}^{0} \langle u \rangle M^2 \, dz = -\frac{\tau_y^w M^2}{\rho_0 f}, \tag{16}$$

which is valid if the Ekman transport is fully contained within the low PV layer $-H < z < 0$. In this limit, the frictional PV flux resulting from a downfront wind stress is equivalent to the PV flux that would be associated with a surface buoyancy flux of B_{wind} acting over the Ekman layer depth (Thomas 2005).

One important distinction between buoyancy-forced convection and convection induced by a downfront wind stress is the vertical profile of $\langle w'b' \rangle$. In classical upright convection, the buoyancy flux is nearly linear in z and is at maximum just below the surface diffusive boundary layer (Deardorff et al. 1969). In the case of downfront

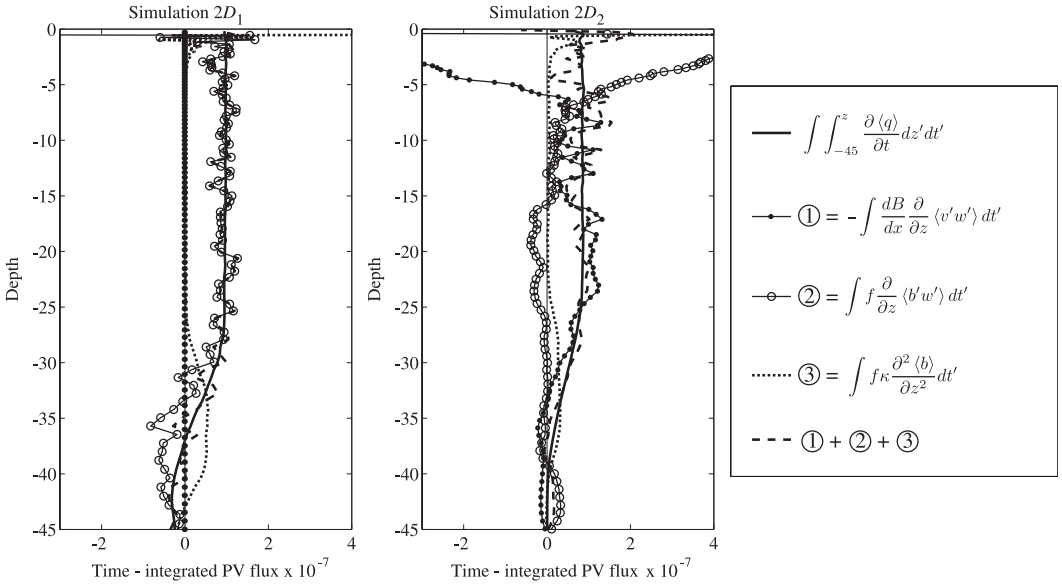

FIG. 10. PV budget with the advective PV flux approximated by Eq. (14) for (left) $2D_1$ and (right) $2D_2$. The time integral is applied over $150 < t < 300$ h.

winds, the profile of the effective buoyancy flux depends on the velocity profile in the turbulent Ekman layer. Because the velocity profile is itself modified by turbulence created by destabilizing the water column, predicting the vertical structure of the effective buoyancy flux is not trivial. To compare buoyancy-forced convection to a downfront wind stress, one additional simulation ($2D_7$) includes a downfront wind stress and no surface buoyancy loss. Simulation $2D_7$ has the same horizontal density gradient as simulation $2D_2$, and the wind stress is prescribed so that the integrated effective buoyancy flux B_{wind} matches B_0 for simulation $2D_2$; that is, $\tau_y^w/\rho_0 = -B_0 f/M^2$.

A visualization from simulation $2D_7$ is shown in the bottom panel of Fig. 6. Like simulation $2D_2$, the streamlines in the low PV layer are nearly aligned with the isopycnals. It appears that the same dynamics seen for slantwise convection forced are active in simulation $2D_7$; forced SI develops in response to the surface forcing, and shear instabilities lead to vertical mixing inside the low PV layer. Unlike simulation $2D_2$, a sharp surface density front is visible in simulation $2D_7$. Several isopycnals outcrop at this front, which also appears to be linked to the circulation cells. This circulation is very similar to that described by Thomas and Lee (2005). The surface Ekman flow is highly convergent at the front; one side of the front has a stable density profile but the other is convectively unstable, and the streamlines are approximately aligned with the isopycnals beneath the front. One apparent difference is that, on the stable side of the front, the isopycnals in our simulation $2D_7$ are aligned with the streamfunction, whereas in Thomas and Lee (2005) the isopycnals are roughly perpendicular to the streamfunction.

5. 3D large-eddy simulations

The previous sections presented results from numerical simulations where variations in the alongfront (y) direction were neglected. Because some properties of turbulent convection are different in two and three dimensions (see, e.g., Moeng et al. 2004), we have repeated simulations $2D_1$ and $2D_2$ using three-dimensional large-eddy simulations (LES). The computational domain size for the 3D simulations is $L_x = 1000$ m, $L_y = 250$ m, $L_z = 50$ m. The resolution in the 3D simulations is lower than the 2D simulations with $N_x = 256$, $N_y = 64$, $N_z = 50$ grid points. The grid is stretched in the z direction with a grid spacing of 0.33 m at the upper surface and 1.64 m at the bottom of the domain. A sponge region is placed from -50 m $< z < -40$ m with the same functional form as in the 2D simulations.

The concept behind a large-eddy simulation is to solve a low-pass filtered form of the governing equations. The resolved velocity field is then used to model the subgrid-scale stress tensor $\tau_{i,j}^{\text{SGS}}$, whereas molecular values are used for the explicit viscosity and diffusivity (here $\nu = 1 \times 10^{-6}$ m^2 s^{-1} and $Pr = \nu/\kappa = 7$). We have used the constant Smagorinsky model,

$$\tau_{i,j}^{\text{SGS}} = -2C^2\overline{\Delta}^2|\overline{S}|\overline{S}_{i,j}, \tag{17}$$

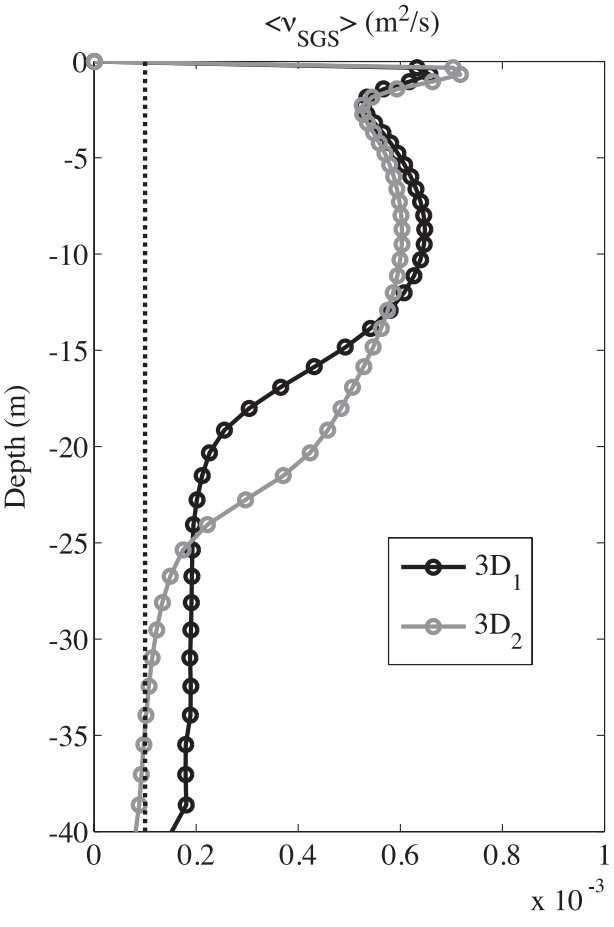

FIG. 11. Subgrid-scale eddy viscosity calculated using the modified constant Smagorinsky model in Eq. (17). The dashed vertical line indicates the constant eddy viscosity that was used in the higher-resolution 2D simulations.

where $\overline{\Delta} = (\Delta_x\Delta_y\Delta_z)^{1/3}$ is the implicit LES filter width and $C = 0.13$ is the Smagorinsky coefficient. The subgrid-scale eddy viscosity from the Smagorinsky model is $\nu_{SGS} = C^2\overline{\Delta}^2|\overline{S}|$, and a constant subgrid-scale Prandtl number $\mathrm{Pr}_{SGS} = \nu_{SGS}/\kappa_{SGS} = 1$ has been applied. Representative profiles of the mean subgrid-scale viscosity are shown in Fig. 11. Note that, unlike the 2D simulations, ν_{SGS} varies in all three spatial directions as well as in time. The constant eddy viscosity used in the 2D simulations is shown as a dotted line in Fig. 11.

The initial flow in our simulations consists of a stratified shear flow with a stable Richardson number. This state presents a well-known problem in LES modeling: the constant Smagorinsky model would yield a nonzero subgrid-scale viscosity, even though the flow is nonturbulent. Kaltenbach et al. (1994) found that by excluding the mean shear from the rate of strain tensor, $|\overline{S}|$ in Eq. (17), the performance of the Smagorinsky model is improved, and we have taken the same approach here. In both $3D_2$ and $3D_1$, the plane-averaged subgrid-scale kinetic energy is always less than 2% of the total turbulent kinetic energy, with the exception of a brief initial transient and the viscous surface layer.

Visualizations of the cross-front velocity and the density field are shown for simulations $3D_2$ and $3D_1$ in Fig. 12. The parameters for simulations $3D_2$ (slantwise convection) and $3D_1$ (upright convection) are identical to those for simulations $2D_1$ and $2D_2$ (see Table 1). The convective plumes in 3D upright convection (simulation $3D_1$) are significantly smaller and less coherent than their 2D counterparts. In contrast, simulations $2D_2$ and $3D_2$ for slantwise convection are qualitatively very similar. Both show along-isopycnal motion in the low PV layer accompanied by intermittent shear instabilities, with a convective layer near the surface. The along-isopycnal structures in simulation $3D_2$ are coherent in the y direction, despite some 3D turbulent fluctuations.

Profiles of the mean PV and Ri_B for both 3D simulations are compared with the 2D simulations in Fig. 13. To minimize statistical noise, these quantities have been averaged over horizontal planes and over one inertial period. Overall, the mean profiles and turbulent features agree remarkably well between the 2D and 3D simulations. In all simulations, a low PV layer with $\mathrm{Ri}_B \simeq 1$ develops, and the depth of this layer is nearly the same for the 2D and 3D simulations. A surface convective layer forms in both $3D_2$ and $2D_2$ where the buoyancy flux is large and the stratification is relatively weak, although the convective layer is slightly deeper in the 3D simulation. Finally, the base of the low PV layer is more diffuse in both 3D simulations compared to their 2D counterparts.

6. Scaling for the depth of the low PV layer

Turbulent convection into a fluid with a stable vertical stratification is a classical problem in the stratified turbulence literature. Although this problem is traditionally viewed in terms of the mean buoyancy equation [Eq. (9)], the mean PV budget [Eq. (11)] is equally valid. When $M^2 \simeq 0$, as in the limit for upright convection, the momentum flux does not contribute to the PV flux in Eq. (14) and the mean PV budget reduces to an evolution equation for $\langle N^2\rangle$ [i.e., the derivative of Eq. (9)]. In this section, we will derive an expression for the depth of the low PV layer using the principle of PV conservation. This has the advantage of naturally incorporating the momentum flux terms that are important in slantwise convection and the role of a surface wind stress.

The classical scaling for the depth of the ML in upright convection, with a constant surface buoyancy flux

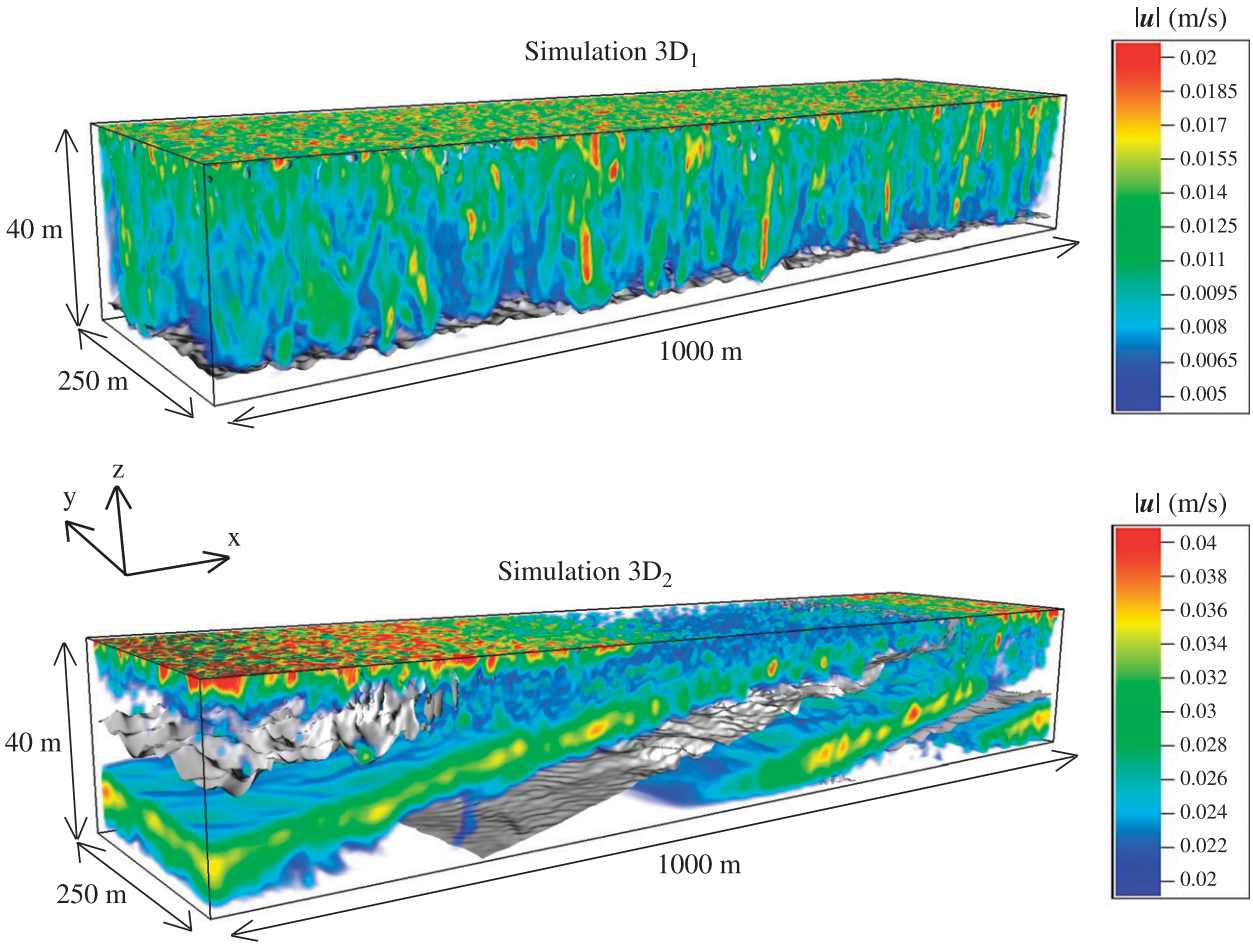

FIG. 12. Velocity magnitude (color) and isopycnals (gray) for simulations (top) $3D_2$ and (bottom) $3D_1$ at $t = 15$ days. Velocity lower than the minimum on each color scale is made transparent.

$B_0 = \kappa db/dz$ into a linearly stratified fluid, is given by (Deardorff et al. 1969)

$$H(t) = \sqrt{\frac{2\alpha B_0 t}{N_0^2}}, \tag{18}$$

where the entrainment coefficient α, as defined in Table 1, accounts for turbulent and diffusive buoyancy fluxes across the ML base. For convection modified by rotation, Levy and Fernando (2002) proposed that $N_0^2 + 4Cf^2$ should replace N_0^2 in the denominator of Eq. (18) where $C \simeq 0.02$ based on experimental data. For the parameters considered in this study, $4Cf^2 \ll N_0^2$, so the influence of rotation in Eq. (18) can be neglected.

Straneo et al. (2002) used a heuristic argument to derive an expression analogous to Eq. (18) including a horizontal density gradient. By assuming that slantwise convection mixes density along surfaces of constant angular momentum, they argued that N_0^2 in the denominator of Eq. (18) should be replaced by $N_0^2 - M^4/f^2$. However, in the forced SI regime, we do not observe coherent convective plumes extending to the base of the low PV layer as assumed by Straneo et al. (2002), so it is not apparent that their scaling will apply in our parameter range.

Recall that, in Eq. (14), the advective vertical PV flux can be related to the time rate of change in the mean buoyancy. This result can be used to relate the PV flux to the surface forcing parameters. Consistent with the scaling for the ML depth in upright convection and with the numerical simulations described earlier, $\partial\langle b\rangle/\partial t$ is assumed independent of z in a low PV layer of depth H. Based on Eq. (14), this is equivalent to asserting that the PV flux is independent of depth in the low PV layer. Integrating Eq. (9) over $-H < z < 0$ gives

$$\begin{aligned} H\frac{d\langle b\rangle}{dt} &= B_0 + \langle w'b'\rangle|_{-H} - \kappa\frac{\partial\langle b\rangle}{\partial z}\bigg|_{-H} - M^2\int_{-H}^{0}\langle u\rangle\, dz \\ &= (1 + \alpha + \beta)(B_0 + B_{\text{wind}}), \end{aligned} \tag{19}$$

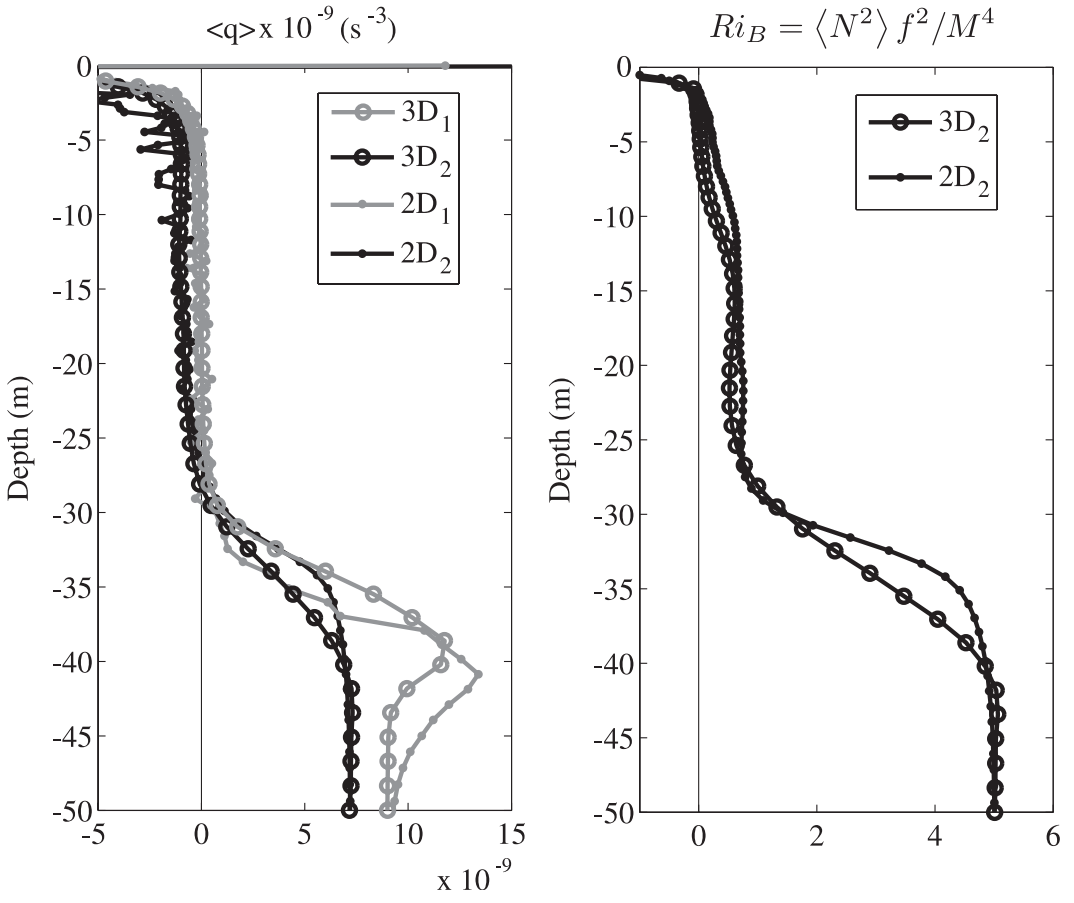

FIG. 13. (left) Mean PV and (right) bulk Richardson number at $t = 10$ days. To reduce the statistical noise, both quantities have been averaged over one inertial period.

where the entrainment coefficient α accounts for the turbulent and diffusive buoyancy flux at $z = -H$. When $M^2 \neq 0$, the PV flux can also be associated with a momentum flux divergence, as seen in Eq. (14). An additional entrainment coefficient β has been introduced to include the effect of the momentum flux at $z = -H$ acting on the lateral buoyancy gradient; $\beta = 0$ in the absence of a front (when $M^2 = 0$). The definitions for α and β are given in Table 1. Substituting Eq. (19) in Eq. (14), the PV flux can be written in terms of the surface forcing,

$$\langle q'w' \rangle_{\mathrm{ML}} = -\frac{f}{H}(1 + \alpha + \beta)(B_0 + B_{\mathrm{wind}}). \qquad (20)$$

With the expression for the PV flux as a function of the surface forcing in Eq. (20), we can use the PV conservation equation to predict the growth rate of the low PV layer. The low PV layer depth $H(t)$ will be defined as the location where the PV flux vanishes. When $M^2 = 0$, this corresponds to the location where the buoyancy flux is at minimum [see Eq. (14)], which is consistent with the traditional definition of the ML base in upright convection. Using this definition of $H(t)$ and integrating the mean PV conservation equation [Eq. (11)] from $-H(t) < z < 0$,

$$\frac{\partial}{\partial t}\left(\int_{-H}^{0} \langle q \rangle \, dz\right) - \frac{dH}{dt}\langle q \rangle|_{-H} = -\langle J_0^z \rangle, \qquad (21)$$

where J_0^z is the surface PV flux defined in Eq. (13) and $\langle J_0^z \rangle \simeq \langle q'w' \rangle_{\mathrm{ML}}$ because the PV flux in the ML is presumed to be constant. Using Eq. (20) to replace $\langle J_0^z \rangle$ in Eq. (21) yields an equation for H in terms of the surface forcing and $\langle q \rangle|_{-H}$, the PV in the thermocline:

$$H\left[\frac{\partial}{\partial t}\left(\int_{-H}^{0} \langle q \rangle \, dz\right) - \frac{dH}{dt}\langle q \rangle|_{-H}\right] = f(1 + \alpha + \beta)(B_0 + B_{\mathrm{wind}}). \qquad (22)$$

When either forced SI or upright convection maintains a low PV layer with $\langle q \rangle_{\mathrm{ML}} \simeq 0$, Eq. (22) simplifies to

$$-H\frac{dH}{dt} = \frac{f(1+\alpha+\beta)}{fN_0^2 - M^4/f}(B_0 + B_{\text{wind}}), \qquad (23)$$

where we have also used $\langle q\rangle|_{-H} = Q_0 = fN_0^2 - M^4/f$ based on the initial conditions used here. If we then neglect the surface wind stress and any entrainment ($\alpha = \beta = 0$), Eq. (23) reduces to the expression derived by Straneo et al. (2002). If we neglect the lateral buoyancy gradient (i.e., $M^2 = 0$), Eq. (23) also limits to the expression for the ML depth derived for classical upright convection given in Eq. (18). Equation (23) is one of the primary contributions of this paper.

The depth of the low PV layer found by integrating Eq. (23) is shown as a dashed line along with the evolution of the mean PV in Figs. 7–9. The depth of the low PV layer is well captured by Eq. (23) with the exception of simulation $2D_4$, which is associated with the largest horizontal density gradient. In this simulation, a layer with a strongly negative PV forms near the surface for $t < 3$ days, and the term in Eq. (22) involving the time rate of change of the integrated PV is nonnegligible. If we wait until the integrated PV becomes steady and integrate Eq. (23), the growth in H is captured well for the rest of the simulation (shown as a thin solid line in Fig. 8).

By examining the values of α and β given in Table 1, it appears that slantwise convection is less effective at entraining fluid into the low PV layer than upright convection. For example, $\alpha + \beta = 0.3$ in simulation $2D_1$ with upright convection, but this sum is nearly zero in simulation $2D_4$ with a deep layer of forced symmetric instability. However, it is difficult to make precise quantitative statements about the values of the entrainment coefficients, because in all 2D and 3D simulations the entrainment buoyancy flux is dominated by the subgrid-scale processes Taylor and Sarkar (2008) found that the Ellison scale provides a good estimate for the entrainment length scale. In simulation $2D_2$, the Ellison scale at the base of the mixed layer is $L_E \equiv \langle b'^2\rangle^{1/2}/(d\langle b\rangle/dz) \simeq 0.2$ m, so very high–resolution simulations would be needed to resolve the entrainment process.

7. Scaling of the convective layer depth

We have seen in Eq. (14) and Fig. 10 that the PV flux inside the low PV layer can be associated with either momentum or buoyancy fluxes. When $M^2 = 0$, as in simulation $2D_1$, only the buoyancy flux term contributes to the PV flux. In contrast, when forced SI is active as in the interior of the low PV layer in simulation $2D_2$, the PV flux is dominated by the momentum flux term. However, even in this case, the buoyancy flux term is still important for $z \gtrsim -10$ m. We will refer to this upper region as the convective layer, because convective plumes are visible in this layer and the stratification is relatively weak compared to the forced SI layer. When M^2 is reduced, the buoyancy flux penetrates deeper into the low PV layer, resulting in a deeper convective layer. Forced SI is seen only below the convective layer but within the low PV layer: that is, for $-H \le z \le -h$, where h is the convective layer depth defined as the location where $\langle w'b'\rangle = 0$. The relative sizes of h and H will, therefore, determine whether a forced SI layer can form for a given set of parameters. The objective of this section is to derive a scaling for h based on the external parameters.

Start by integrating the mean buoyancy equation [Eq. (9)] from $z = -h$ to $z = 0$,

$$\int_{-h}^{0}\frac{\partial\langle b\rangle}{\partial t} + M^2\int_{-h}^{0}\langle u\rangle\, dz = B_0, \qquad (24)$$

using the definition of h to assert that $\langle w'b'\rangle|_{-h} = 0$ and neglecting the diffusive buoyancy flux at $z = -h$. If, as in section 6, we assume that $\partial\langle b\rangle/\partial t$ is independent of z in the low PV layer, then Eq. (24) can be rewritten as

$$M^2\int_{-h}^{0}\langle u\rangle\, dz = B_0 - (1+\alpha+\beta)\frac{h}{H}(B_0 + B_{\text{wind}}), \qquad (25)$$

where we have used the expression for $d\langle b\rangle/dt$ from Eq. (19) and the definition of B_{wind} from Eq. (16).

Integrating the steady y-momentum equation between the same limits gives

$$f\int_{-h}^{0}\langle u\rangle\, dz = \langle v'w'\rangle_{-h} + \tau_y^w/\rho_0, \qquad (26)$$

where we have neglected the molecular viscous stress at $z = -h$. We can combine Eqs. (25) and (26) to form a scaling for h given an estimate for the alongfront momentum flux at the base of the convective layer $\langle v'w'\rangle_{-h}$. To estimate the scaling for this term, we will introduce separate turbulent velocity scales w_* and v_*. For the vertical velocity fluctuations, we will use the convective scaling $w_* \sim [(B_0 + B_{\text{wind}})h]^{1/3}$. If we assume that for $z > -h$, alongfront velocity fluctuations are caused by convective mixing of the thermal wind shear, then a natural scaling is $v_* \sim h(dV_G/dz) = hM^2/f$. Combining these velocity scales gives a scaling for the momentum flux $\langle v'w'\rangle_{(z=-h)} \sim v_*w_* \sim h(M^2/f)[(B_0 + B_{\text{wind}})h]^{1/3}$. Using this scaling in Eqs. (25) and (26) then yields an implicit expression for the convective layer depth,

$$\frac{M^4}{f^2}(B_0 + B_{\text{wind}})^{1/3}h^{4/3} = c\left\{(B_0 + B_{\text{wind}})\left[1 - (1 + \alpha + \beta)\frac{h}{H}\right]\right\}. \quad (27)$$

Note that, in the limit of $M^2 = 0$ for upright convection without a mean horizontal velocity, it is reasonable to assume that the Reynolds stress $\langle v'w' \rangle \simeq 0$. In this case, the convective layer depth inferred from Eq. (27) matches the depth where a linear buoyancy flux profile crosses zero, which is consistent with the definition of h.

For sufficiently deep convective layers, the convective scaling for the vertical velocity used in Eq. (27) would also need to be modified by rotation (see, e.g., Jones and Marshall 1993). This occurs when the convective Rossby number $\text{Ro} = (B_0^{1/2}/f^{3/2}h) < 1$, where $B_0 = \kappa db/dz_{z=0}$ is the surface buoyancy flux and h is the convective layer depth. The deepest convective layer considered here is $h \simeq 50$ m in simulation $2D_1$, corresponding to a convective Rossby number of $\text{Ro} \simeq 4.1$. Therefore, although rotation always plays a role in symmetric instability, it does not directly impact the convective plumes in this study.

Evaluating the scaling factor c in Eq. (27) based on the location where $\langle w'b' \rangle \simeq 0$ in the 2D simulations gives $c \simeq 13.9$. As seen in Fig. 14a, Eq. (27) appears to capture the convective layer depth defined as the location where $\langle w'b' \rangle = 0$ for various values of B_0 and M^2. In the forced SI layer, for $-H < z < -h$, the buoyancy flux is generally either small or negative, indicating that this layer is not convective in the traditional sense. Using the parameters from Straneo et al. (2002) in Eq. (27) gives a convective layer depth of $h \simeq 900$ m. Because h is nearly equal to the low PV layer depth of $H \simeq 1000$ m, this likely explains why forced SI was not observed in Straneo et al. (2002).

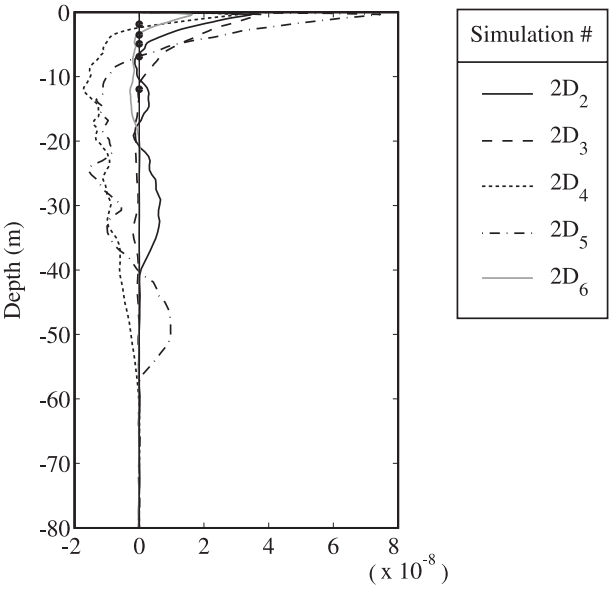

FIG. 14. Mean buoyancy flux profiles. Averages have been taken in x and t for one inertial period centered at $t = 15$ days. Dots show the scaling derived in Eq. (27) with an empirical constant of $c = 13.9$.

8. TKE budget

In upright convection, the turbulent buoyancy flux $\langle w'b' \rangle$ acts as the dominant source of TKE at the expense of potential energy. We have seen that, in the case of slantwise convection, the turbulent buoyancy flux can effectively vanish inside the low PV layer (see Fig. 10). This raises the question, is the low PV layer turbulent? If so, how is turbulence maintained? To address these questions, it is useful to introduce the TKE budget,

$$\frac{\partial \langle k \rangle}{\partial t} = \underbrace{-\frac{\partial}{\partial z}\left(\langle w'k' \rangle + \frac{1}{\rho_0}\langle w'p' \rangle - \nu\frac{\partial \langle k \rangle}{\partial z}\right)}_{\text{Transport}} \underbrace{- \langle u'w' \rangle \frac{\partial \langle u \rangle}{\partial z} - \langle v'w' \rangle \frac{\partial \langle v \rangle}{\partial z} - \langle v'w' \rangle \frac{dV_G}{dz}}_{\text{Shear production}}$$
$$+ \underbrace{\langle w'b' \rangle}_{\text{PE Conversion}} + \underbrace{\langle \mathbf{u} \cdot (\nabla \cdot \boldsymbol{\tau}^{\text{SGS}}) \rangle}_{\text{SGS work}} \underbrace{-\epsilon}_{\text{Dissipation}}, \quad (28)$$

where $k = \frac{1}{2}(u'^2 + v'^2 + w'^2)$ is the TKE, $\epsilon = 2\nu\langle s'_{i,j}s'_{i,j} \rangle$ is the turbulent dissipation rate, and $s'_{i,j} \equiv (\partial u'_i/\partial x_j + \partial u'_j/\partial x_i)/2$ is the rate of strain tensor.

The shear production terms in Eq. (28) have been separated into terms involving the geostrophic and ageostrophic mean shear. It can be shown that the ageostrophic terms do not generate TKE in a depth-integrated sense. Using the inviscid form of the Ekman balance given in Eq. (10), the ageostrophic shear production can be written

$$P_{\text{AG}} = -\langle u'w' \rangle \frac{\partial \langle u \rangle}{\partial z} - \langle v'w' \rangle \frac{\partial \langle v \rangle}{\partial z} \simeq \frac{1}{f}\frac{\partial}{\partial z}\left(-\frac{\partial \langle v'w' \rangle}{\partial z}\langle u'w' \rangle + \langle v'w' \rangle \frac{\partial \langle u'w' \rangle}{\partial z}\right). \quad (29)$$

In the absence of surface waves, $\langle u'w' \rangle$ and $\langle v'w' \rangle$ vanish at $z = 0$. If we also neglect the momentum flux carried by internal waves into the thermocline, the vertical integral of Eq. (29) is approximately zero. In this case, P_{AG} does

not contribute to the depth-integrated TKE and represents the redistribution of TKE by the momentum stress terms.

Now, consider the geostrophic turbulent production term $P_G = -\langle v'w'\rangle(dV_G/dz) = -M^2\langle v'w'\rangle/f$. We can integrate the alongfront mean Ekman balance from Eq. (10) to relate the turbulent momentum flux $\langle v'w'\rangle$ to the cross-front velocity,

$$\langle v'w'\rangle + \tau_y^w/\rho_0 - f\int_z^0 \langle u\rangle\, dz' = 0. \tag{30}$$

The integrated cross-front velocity can be reexpressed in terms of the buoyancy flux by integrating the mean buoyancy equation [Eq. (9)] over the same interval,

$$M^2\int_z^0 \langle u\rangle\, dz' = \langle w'b'\rangle|_z + \frac{z}{H}(B_0 + B_{\text{wind}})(1+\alpha+\beta) + B_0, \tag{31}$$

where we have assumed that $\partial\langle b\rangle/\partial t$ is independent of z as in Eq. (19) and we have neglected the diffusive buoyancy flux at z. The geostrophic production can then be written as

$$P_G = -\frac{M^2}{f}\langle v'w'\rangle = -\langle w'b'\rangle - (B_0 + B_{\text{wind}})\left[1 + \frac{z}{H}(1+\alpha+\beta)\right]. \tag{32}$$

Therefore, the geostrophic production plus the buoyancy flux is a linear function of z. This statement is true regardless of the size of M^2 and whether the front is forced by winds or a surface buoyancy flux. Therefore, in the forced SI layer, where the buoyancy flux is less than or equal to zero, the geostrophic production must compensate to keep $P_G + \langle w'b'\rangle$ the same as in upright convection. Although turbulent production is maintained in both upright and slantwise convection, the relative sizes of $\langle w'b'\rangle$ and P_G determine the ultimate source of TKE in the system. When $\langle w'b'\rangle > 0$, TKE is generated at the expense of the mean potential energy generated by the surface buoyancy flux. In contrast, the geostrophic production term represents energy extracted from the thermal wind shear. Although our simulations keep the strength of the front fixed in time, extracting energy from the thermal wind shear could be expected to lead to a geostrophic adjustment and a slumping of the front in a freely evolving system. Geostrophic production, which is active in forced SI, therefore represents a pathway through which available potential energy associated with the tilting isopycnals of the front can be converted to TKE, which will either be dissipated through friction or used to mix the vertical stratification.

Note that, although Eq. (27) includes the wind-induced buoyancy flux, the scaling for $\langle v'w'\rangle|_{-h}$ introduced in section 7 does not include turbulence generated directly by the wind stress. The Obukhov length $L \equiv u_*^3/(\kappa B_0)$ is a measure of the relative importance of shear and buoyancy forcing, where $u_* = \sqrt{\tau^w/\rho_0}$. Monin–Obukhov similarity theory (Monin and Obukhov 1954) states that, when $|z/L|$ is small, shear production and viscous diffusion dominate buoyancy effects, whereas, when z/L is large and negative, the flow becomes independent of u_* and L and convective scaling is valid. This suggests that we can use the Obukhov length L along with the convective layer depth h to separate the low PV layer into three regions: for $z > O(-L)$, turbulence is dominated by the wind stress; for $-h < z < O(-L)$, a convective layer exists, where turbulence is produced by the combined buoyancy fluxes $B_0 + B_{\text{wind}}$; and for $-H < z < -h$, a forced SI layer can be expected. In simulation $2D_7$, the Obukhov length $L \simeq 1.8$ m; indeed, shear production and viscous diffusion dominate the turbulent kinetic energy budget for $z > -2$ m, the buoyancy flux is large and positive for -2 m $< z < -8$ m, and a forced SI region is present for $z < -8$ m.

9. Discussion

We have described numerical simulations for slantwise convection near the ocean surface forced by either a surface buoyancy loss or a downfront wind stress. Regardless of the strength of the horizontal density gradient, a region of low PV develops, and the depth of this layer has been derived using mean PV conservation. Integrating Eq. (23) gives

$$H(t) = \left[H_0^2 + \frac{2ft}{fN_0^2 - M^4/f}(1+\alpha+\beta)\left(B_0 - \frac{\tau_y^w M^2}{\rho_0 f}\right)\right]^{1/2}, \tag{33}$$

where N_0 is the buoyancy frequency at $t = 0$, $M^2 = db/dx$ is the lateral buoyancy gradient, B_0 is the surface buoyancy flux, τ_y^w is the wind stress in the alongfront direction, H_0 is the low PV layer depth at $t = 0$, and α and β are entrainment coefficients defined in Table 1. Equation (33) limits to the expression first derived by Deardorff et al. (1969) for upright convection when $M^2 = 0$. In writing Eq. (33), we have assumed that the PV associated with the front is constant and can be written as $Q_0 = fN_0^2 - M^4/f$. If the background PV is depth or time dependent or if it is affected by other terms including a relative

vorticity, then Eq. (22) can be integrated to obtain a more general expression for the low PV layer depth.

Two limiting dynamical regimes of slantwise convection have been identified based on the relative importance of the turbulent buoyancy flux. Near the surface, a convective layer forms where the buoyancy flux is positive and the stratification is relatively weak. When the horizontal density gradient is sufficiently large, a new dynamical regime called "forced symmetric instability" (forced SI) occurs beneath the convective layer. In the forced SI region, a vertical stratification develops so that the bulk Richardson number is nearly neutral with respect to SI. Also, as in SI, a flow develops that is nearly aligned with the tilted isopycnal surfaces and independent of the alongfront direction. Turbulence is generated through shear instabilities, and the buoyancy flux is no longer the dominant source of turbulent kinetic energy.

It is common for one-dimensional ML models to parameterize turbulent fluxes in terms of a bulk Richardson number (Phillips 1977; Pollard et al. 1973; Price et al. 1986). We have seen that forced SI maintains $\mathrm{Ri}_B = N^2 f^2 / M^4 \simeq 1$, which is the neutral state for SI. If most of the shear in the ML is in balance with an existing front, forced SI might provide a physical basis for using a bulk Richardson number criterion in ML models. It is also worth considering how the scaling theory presented in sections 6 and 7 applies to observed ML fronts. Consider, for example, the outcropping Azores front observed by Rudnick and Luyten (1996). It is convenient that, when $\alpha + \beta = 0$, the ratio h/H, formed from Eqs. (23) and (27), is independent of B_0. Using parameters estimated from Rudnick and Luyten (1996; $N^2 \simeq 3.7 \times 10^{-5}\ \mathrm{s}^{-2}$, $M^{-2} \simeq 2.5 \times 10^{-7}\ \mathrm{s}^{-2}$, and $f \simeq 8 \times 10^{-5}\ \mathrm{s}^{-1}$) in these equations gives $h/H \simeq 0.4$ at $t = 2$ days. Although the surface fluxes were not reported in Rudnick and Luyten (1996), the scaling analysis implies that, if PV was removed from this front via a surface buoyancy loss or a downfront wind stress, forced SI would likely occur in a large fraction of the low PV layer.

The simulations presented here were designed to isolate the influence of a horizontal buoyancy gradient on buoyancy and wind-driven convection. As a result, numerous physical processes that are important to mixed layer dynamics have not been included. For example, the influence of surface waves, including wave breaking and Langmuir circulation, may influence both the mixed layer depth H and the convective layer depth h, particularly when the flow is driven by a wind stress. We have also not explicitly considered the influence of unbalanced motions such as inertial oscillations or internal waves on the flow evolution. An analysis of linear symmetric instability developing from a background flow that contains an ageostrophic component seems like an obvious extension of the present study. Clearly, there are many fundamental questions left to be addressed in future studies.

The numerical simulations that have been presented here have been run for 10–20 days, and most results have been reported at $t = 15$ days, a long enough time for some of the assumptions made here to break down in practice. For example, ML baroclinic instabilities can become finite amplitude on time scales of days, and it is also unlikely that the surface forcing (either a buoyancy flux or wind stress) would be constant over such a long time period. The large integration time is a direct consequence of the idealized initial conditions. To simplify the initial conditions and to reduce the number of external parameters, we have initialized the simulations with a large constant stratification throughout the entire fluid volume. As a result, there is a significant spinup period needed before a ML develops with a realistic depth based on the forcing level. For example, in simulations $2\mathrm{D}_1$ and $2\mathrm{D}_2$, it takes about 10 days for the low PV layer depth to reach 35 m. Because forced SI requires the convective depth h to be smaller than the low PV layer depth H, a long integration is necessary to observe forced SI, even though SI can reach finite amplitude in less than a day once $H > h$. In the ocean, when a preexisting low PV layer is forced with a surface PV loss, forced SI could develop much faster.

Our objective has been to examine the influence of a horizontal density gradient on turbulent convection, and our domain size has been set so that we are able to resolve the largest three-dimensional turbulent overturns on scales of O(1m). Because of this resolution requirement, the domain size was not large enough to accommodate ML baroclinic instability, which occurs on larger spatial scales than SI. Because the growth rate of SI is faster than baroclinic instability for $Ri_B < 0.95$ (Stone 1966), SI is likely to occur before baroclinic instability. However, the criterion for baroclinic instability depends on gradients in PV, unlike SI, which occurs when the PV is negative. Therefore, a front that has been made neutral with respect to SI can still be unstable to a subsequent baroclinic instability. The baroclinic instability would further restratify the low PV layer by entraining high PV from the thermocline. A topic of future research is to investigate whether baroclinic instability can ever overcome forced SI during times of surface PV loss.

Acknowledgments. This research was supported by ONR Grant N000140910458 (RF) and an NSF Mathematical Sciences Postdoctoral Research Fellowship (JRT). We thank Leif Thomas for many helpful discussions.

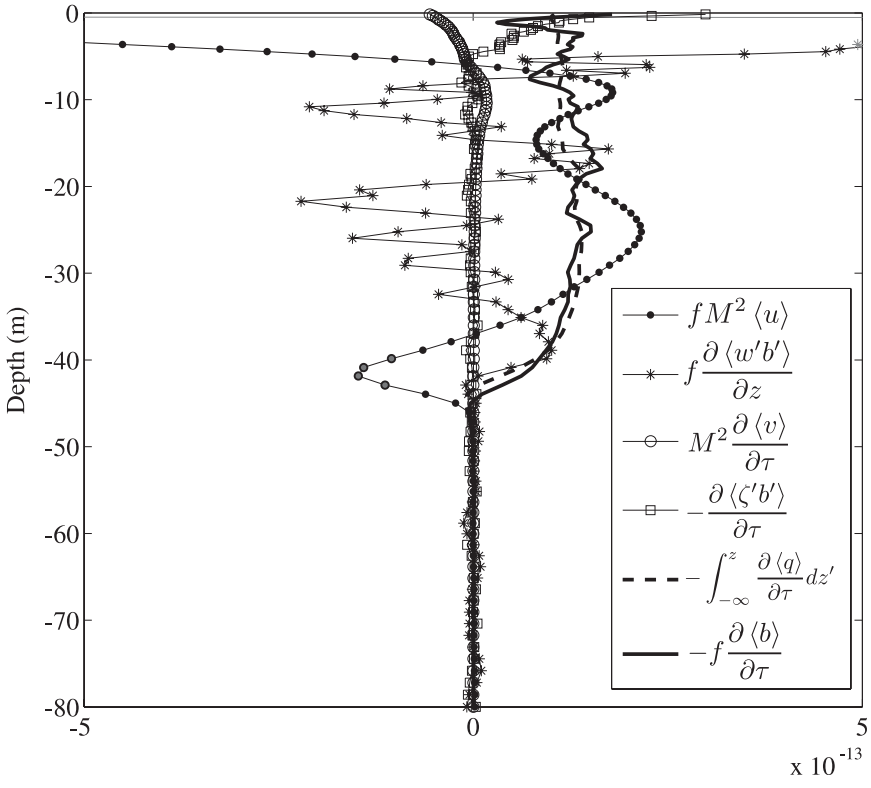

FIG. A1. Inviscid PV flux terms from Eq. (A5) for simulation $2D_2$. Angle brackets denote an average in x and t for one inertial period, centered at $t = 15$ days.

APPENDIX

Scaling of the PV Budget

Consider the potential vorticity in its flux form,

$$q = \frac{\partial}{\partial z}[b(f+\zeta)] + \nabla_H \cdot \left(b\mathbf{k} \times \frac{\partial \mathbf{u}}{\partial z}\right), \qquad \text{(A1)}$$

where $\zeta = \partial v/\partial x - \partial u/\partial y$ is the vertical component of the relative vorticity. The convectively driven low PV layer is actively turbulent and contains frequent density overturns. As a result, the PV exhibits large variations on small space and time scales and the local Rossby number ζ/f is not small. However, the mean PV is more regular, and we can simplify the mean PV budget in the dynamical regimes of interest here.

Define the averaging operator $\langle\cdot\rangle$ to act over x and y and over a fast time scale t. The mean PV can be written as

$$\langle q\rangle = f\frac{\partial\langle b\rangle}{\partial z} + \frac{\partial}{\partial z}\langle\zeta' b'\rangle - M^2\frac{\partial\langle v_T\rangle}{\partial z}. \qquad \text{(A2)}$$

Note that the cross-front shear $\partial\langle u\rangle/\partial z$ does not appear in the last term in Eq. (A2) because the front is aligned with the x axis and the density difference across the domain in the y direction is therefore taken to be zero.

Using Eq. (A2) in the inviscid PV conservation equation and integrating in z gives

$$f\frac{\partial\langle b\rangle}{\partial\tau} + \frac{\partial\langle\zeta' b'\rangle}{\partial\tau} - M^2\frac{\partial\langle v_T\rangle}{\partial\tau} + \langle q'w'\rangle = -C(\tau), \qquad \text{(A3)}$$

where τ is a slow time scale. Applying the same averaging operator to the buoyancy equation, we have

$$\frac{\partial\langle b\rangle}{\partial\tau} + M^2\langle u\rangle + \frac{\partial}{\partial z}\langle w'b'\rangle = 0. \qquad \text{(A4)}$$

Equations (A3) and (A4) can then be combined to yield an expression for the mean PV flux,

$$\langle q'w'\rangle = fM^2\langle u\rangle + f\frac{\partial}{\partial z}\langle w'b'\rangle + M^2\frac{\partial\langle v_T\rangle}{\partial\tau} - \frac{\partial}{\partial\tau}\langle\zeta' b'\rangle. \qquad \text{(A5)}$$

The constant of integration in Eq. (A5) was set to zero, assuming that the PV flux vanishes in the thermocline. Consider the following scaling applied to the two regimes observed in slantwise convection:

$$x \sim l, \quad z \sim h, \quad \tau \sim \tau_0, \quad \langle \mathbf{u}_T\rangle \sim U, \quad u', v' \sim u,$$
$$w' \sim w, \quad b' \sim B_0/w.$$

a. Convective layer, $z > -h$

Here, by definition, the buoyancy flux is a leading order term in the buoyancy budget, implying that $M^2U \leq O(B_0/h)$. Using the scaling defined here, the ratio of the third to the second term on the right-hand side of Eq. (A5) is

$$\frac{M^2Uh}{B_0\tau_0 f} \leq O(\tau_0 f)^{-1} \tag{A6}$$

and the ratio of the fourth term in Eq. (A5) to the buoyancy flux term is

$$\frac{uh}{wl\tau_0 f} \sim (\tau_0 f)^{-1}, \tag{A7}$$

where we have used $w/h \sim u/l$ from the continuity equation. Therefore, the last two terms in the mean PV flux can be neglected compared to the buoyancy flux term in the convective layer when $\tau_0 f \gg 1$.

b. Forced SI

In this limit, the cross-front advection term $M^2\langle u\rangle$ dominates over the buoyancy flux term. Comparing the ratios of the last two terms in Eq. (A5) to the cross-front advection term,

$$\frac{M^2U}{\tau_0 fM^2U} = (\tau_0 f)^{-1} \quad \text{and} \tag{A8}$$

$$\frac{uB_0}{wlM^2U\tau_0 f} \sim \frac{B_0}{hM^2U\tau_0 t} < \frac{M^2U}{M^2U\tau_0 f} = (\tau_0 f)^{-1}. \tag{A9}$$

Therefore, in both of the limits of interest here, the last two terms in Eq. (A5) can be neglected compared to the larger of the first two terms, as long as the averaging interval is large compared to the inertial period. Neglecting these terms, the mean PV flux is approximately

$$\langle q'w'\rangle \simeq fM^2\langle u\rangle + f\frac{\partial}{\partial z}\langle w'b'\rangle \simeq -f\frac{\partial\langle b\rangle}{\partial\tau}. \tag{A10}$$

The individual contributions to the PV flux are shown in Fig. A1 for simulation $2D_2$. Because variations in the y direction are neglected in this simulation, $\zeta = \partial v/\partial x$. Profiles of the PV flux are very noisy, so instead we plot the vertical integral of $\partial\langle q\rangle/\partial\tau$, which is equal to $\langle q'w'\rangle$ when $\nu = \kappa = 0$ [see Eq. (11)]. Note that the average operator was applied for one inertial period, so the criterion $(\tau_0 f)^{-1} \ll 1$ is not strictly satisfied. Nevertheless, with the exception of a relatively thin region near the surface, last two terms in Eq. (A5) are small and Eq. (A10) is a good approximation.

REFERENCES

Bewley, T., 2010: *Numerical Renaissance: Simulation, Optimization, and Control*. Renaissance Press, in press.

Boccaletti, G., R. Ferrari, and B. Fox-Kemper, 2007: Mixed layer instabilities and restratification. *J. Phys. Oceanogr.,* **37,** 2228–2250.

Deardorff, J., G. Willis, and D. Lilly, 1969: Laboratory investigation of non-steady penetrative convection. *J. Fluid Mech.,* **35,** 7–31.

Haine, T., and J. Marshall, 1998: Gravitational, symmetric, and baroclinic instability of the ocean mixed layer. *J. Phys. Oceanogr.,* **28,** 634–658.

Jones, H., and J. Marshall, 1993: Convection with rotation in a neutral ocean: A study of open-ocean deep convection. *J. Phys. Oceanogr.,* **23,** 1009–1039.

Kaltenbach, H.-J., T. Gerz, and U. Schumann, 1994: Large-eddy simulation of homogeneous turbulence and diffusion in a stably stratified shear flow. *J. Fluid Mech.,* **280,** 1–41.

Levy, M., and H. Fernando, 2002: Turbulent thermal convection in a rotating stratified fluid. *J. Fluid Mech.,* **467,** 19–40.

Marshall, J. C., and J. G. Nurser, 1992: Fluid dynamics of ocean thermocline ventilation. *J. Phys. Oceanogr.,* **22,** 583–595.

——, and F. Schott, 1999: Open-ocean convection: Observations, theory, and models. *Rev. Geophys.,* **37,** 1–64.

Moeng, C.-H., J. McWilliams, R. Rotunno, P. Sullivan, and J. Weil, 2004: Investigating 2D modeling of atmospheric convection in the PBL. *J. Atmos. Sci.,* **61,** 889–903.

Monin, A., and A. Obukhov, 1954: Basic laws of turbulent mixing in the ground layer of the atmosphere. *Tr. Akad. Nauk SSSR Geol. Inst.,* **24,** 163–187.

Phillips, O., 1977: *The Dynamics of the Upper Ocean*. Cambridge University Press, 336 pp.

Pollard, R., P. Rhines, and R. Thompson, 1973: The deepening of the wind-mixed layer. *Geophys. Fluid Dyn.,* **3,** 381–404.

Price, J., R. Weller, and R. Pinkel, 1986: Diurnal cycling: Observations and models of the upper ocean response to diurnal heating, cooling, and wind mixing. *J. Geophys. Res.,* **91** (C7), 8411–8427.

Rudnick, D., and J. Luyten, 1996: Intensive surveys of the Azores front: 1. Tracers and dynamics. *J. Geophys. Res.,* **101** (C1), 923–939.

Stone, P., 1966: On non-geostrophic baroclinic stability. *J. Atmos. Sci.,* **23,** 390–400.

Straneo, F., M. Kawase, and S. Riser, 2002: Idealized models of slantwise convection in a baroclinic flow. *J. Phys. Oceanogr.,* **32,** 558–572.

Tandon, A., and C. Garrett, 1995: Geostrophic adjustment and restratification of a mixed layer with horizontal gradients above a stratified layer. *J. Phys. Oceanogr.,* **25,** 2229–2241.

Taylor, J., 2008: Numerical simulations of the stratified oceanic bottom boundary layer. Ph.D. thesis, University of California, San Diego, 212 pp.

——, and S. Sarkar, 2008: Direct and large eddy simulations of a bottom Ekman layer under an external stratification. *Int. J. Heat Fluid Flow,* **29,** 721–732.

——, and R. Ferrari, 2009: On the equilibration of a symmetrically unstable front via a secondary shear instability. *J. Fluid Mech.,* **622,** 103–113.

Thomas, L., 2005: Destruction of potential vorticity by winds. *J. Phys. Oceanogr.,* **35,** 2457–2466.

——, and C. Lee, 2005: Intensification of ocean fronts by downfront winds. *J. Phys. Oceanogr.,* **35,** 1086–1102.

Thorpe, A., and R. Rotunno, 1989: Nonlinear aspects of symmetric instability. *J. Atmos. Sci.,* **46,** 1285–1299.

Turner, J. S., 1973: *Buoyancy Effects in Fluids*. Cambridge University Press, 367 pp.